


8-1-2016

Forcing Cesium into Higher Oxidation States via Useful Hard X-ray Induced Chemistry at Extreme Conditions

Daniel Thomas Sneed
University of Nevada, Las Vegas

Follow this and additional works at: <https://digitalscholarship.unlv.edu/thesesdissertations>

 Part of the [Chemistry Commons](#), [Engineering Science and Materials Commons](#), [Materials Science and Engineering Commons](#), and the [Physics Commons](#)

Repository Citation

Sneed, Daniel Thomas, "Forcing Cesium into Higher Oxidation States via Useful Hard X-ray Induced Chemistry at Extreme Conditions" (2016). *UNLV Theses, Dissertations, Professional Papers, and Capstones*. 2807.
<http://dx.doi.org/10.34917/9302965>

This Thesis is protected by copyright and/or related rights. It has been brought to you by Digital Scholarship@UNLV with permission from the rights-holder(s). You are free to use this Thesis in any way that is permitted by the copyright and related rights legislation that applies to your use. For other uses you need to obtain permission from the rights-holder(s) directly, unless additional rights are indicated by a Creative Commons license in the record and/or on the work itself.

This Thesis has been accepted for inclusion in UNLV Theses, Dissertations, Professional Papers, and Capstones by an authorized administrator of Digital Scholarship@UNLV. For more information, please contact digitalscholarship@unlv.edu.

FORCING CESIUM INTO HIGHER OXIDATION STATES VIA *USEFUL HARD X-
RAY INDUCED CHEMISTRY* AT EXTREME CONDITIONS

By

Daniel Sneed

Bachelor of Science – Physics
University of Nevada, Las Vegas
August 2014

A thesis submitted in partial fulfillment
of the requirements for the

Master of Science – Physics

Department of Physics and Astronomy
College of Sciences
The Graduate College

University of Nevada, Las Vegas
August 2016

Copyright 2016 by Daniel Sneed

All Rights Reserved



Thesis Approval

The Graduate College
The University of Nevada, Las Vegas

July 8, 2016

This thesis prepared by

Daniel Sneed

entitled

Forcing Cesium into Higher Oxidation States Via Useful *Hard X-Ray Induced Chemistry*
at Extreme Conditions

is approved in partial fulfillment of the requirements for the degree of

Master of Science – Physics
Department of Physics and Astronomy

Michael Pravica, Ph.D.
Examination Committee Chair

Kathryn Hausbeck Korgan, Ph.D.
Graduate College Interim Dean

John Farley, Ph.D.
Examination Committee Member

Andrew Cornelius, Ph.D.
Examination Committee Member

David W. Hatchett, Ph.D.
Graduate College Faculty Representative

Abstract

FORCING CESIUM INTO HIGHER OXIDATION STATES VIA USEFUL *HARD X-RAY INDUCED CHEMISTRY* UNDER HIGH PRESSURE

By

Daniel Sneed

Dr. Michael Pravica, Thesis Defense Committee Chair
University of Nevada, Las Vegas

Recent theoretical work published in *Nature Chemistry* postulates the existence of cesium in high oxidation states when bonding with fluorine. It is thus predicted to behave as a p-block element (such as xenon) at pressures above 5 GPa. At these pressures, fluorine atoms may bond with the inner p-shell electrons forming CsF_n , where n may vary from 2 up to 6; thus the oxidation state of Cs may change up to 6+. My research focused on physically synthesizing these compounds and to verify that, given the right conditions, bonding doesn't only occur with valence electrons, but with the inner p-shell electrons as well, much like what occurs in xenon chemistry. The difficulty of proving this experimentally is that working with fluorine is extremely difficult and dangerous, and has only been studied at high pressure in one earlier study. For the past two years our group has been working on developing a new field of science we call: *Useful Hard X-ray Photochemistry*. By utilizing the highly penetrating, highly focused, and highly ionizing characteristics of hard x-rays, we can decompose relatively safe and inert solid and liquid samples into simple molecules. We have successfully used our technique to

produce O_2 , H_2 , N_2 , Cl_2 , and most recently F_2 *in situ* within a diamond anvil cell. We have also successfully and safely combusted O_2 and H_2 into water by creating a segregated mixture of potassium perchlorate and ammonia borate within a diamond anvil cell.

We have developed a new method to produce molecular fluorine *in situ*, giving us a safe mechanism to supply excess fluorine that is available to react with cesium in order to experimentally verify the theoretical prediction of the unexpected stoichiometries of cesium compounds. By using techniques such as x-ray absorption fine structure spectroscopy, x-ray diffraction, and Raman spectroscopy, coupled with our new techniques of *in situ* hard x-ray photochemistry, we sought to experimentally demonstrate this theoretical behavior of inner shell bonding and open the door to a better understanding of chemical bonding under extreme conditions. This thesis discusses the results of our attempt to synthesize these novel CsF_n ($n>1$) compounds.

Acknowledgments

I would like to thank my advisor Dr. Michael Pravica and members of the UNLV High Pressure Science and Engineering Center for their support and guidance on this project. I would like to thank my committee members Dr. Andrew Cornelius, Dr. John Farley, and Dr. David Hatchett for their advisement and support in this project. I thank the Canadian Light Source and Dr. Ning Chen for all of his help with XAS modeling and data analysis. I would like to thank Dr. Eunja Kim for her help with DFT calculations and all of her help with the interpretation of data. I also thank Melanie White and Quinlan Smith for all of their help with experiments and sample preparation. I thank Dr. Changyong Park at HPCAT, Advanced Photon Source, Argonne National Lab for his help with XANES and diffraction experiments, as well as helping to give the inspiration for this project.

Portions of this work were performed at HPCAT (Sector 16), Advanced Photon Source (APS), Argonne National Laboratory. HPCAT operations are supported by DOE-NNSA under Award No. DE-NA0001974 and DOE-BES under Award No. DE-FG02-99ER45775, with partial instrumentation funding by NSF. APS is supported by DOE-BES, under Contract No. DE-AC02-06CH11357. I acknowledge support from the DOE Cooperative Agreement No. DE-FC08-01NV14049 with the University of Nevada, Las Vegas. I also acknowledge support from the Department of Energy National Nuclear Security Administration under Award Number DE-NA0000979.

Table of Contents

ABSTRACT.....	iii
ACKNOWLEDGMENTS.....	v
LIST OF TABLES.....	ix
LIST OF FIGURES.....	x
LIST OF ACRONYMS.....	xiii
CHAPTER 1: INTRODUCTION.....	1
CHAPTER 2: BACKGROUND.....	3
PREDICTION OF CsF _n (n>1) COMPOUNDS.....	3
USEFUL HARD X-RAY INDUCED CHEMISTRY.....	4
CHAPTER 3: GENERAL THEORY.....	9
CESIUM FLUORIDE.....	9
POTASSIUM TETRAFLUOROBORATE.....	10
DIAMOND ANVIL CELLS.....	10
RUBY FLUORESCENCE.....	13
RAMAN.....	15
CRYSTAL STRUCTURE OF MATERIAL.....	20

X-RAY DIFFRACTION.....	23
EQUATION OF STATE.....	26
X-RAY ABSORPTION SPECTROSCOPY.....	28
CHAPTER 4: EXPERIMENTAL SECTION.....	39
HIGH PRESSURE X-RAY ABSORPTION SPECTROSCOPY EXPERIMENT.....	39
RAMAN SPECTROSCOPY EXPERIMENT.....	42
HIGH PRESSURE X-RAY DIFFRACTION EXPERIMENT.....	45
CHAPTER 5: RESULTS AND DISCUSSION.....	46
INITIAL HIGH PRESSURE X-RAY ABSORPTION EXPERIMENT ON IRRADIATED MIXTURE OF CESIUM FLUORIDE AND POTASSIUM TETRAFLUOROBORATE.....	46
HIGH PRESSURE X-RAY ABSORPTION EXPERIMENT ON PURE CESIUM FLUORIDE.....	50
SECOND HIGH PRESSURE X-RAY ABSORPTION EXPERIMENT ON IRRADIATED MIXTURE OF CESIUM FLUORIDE AND POTASSIUM TETRAFLUOROBORATE.....	56
X-RAY DIFFRACTION STUDY OF MIXTURE OF CESIUM FLUORIDE AND POTASSIUM TETRAFLUOROBORATE AT 64 GPA.....	64
RAMAN EXPERIMENT ON POTENTIAL NOVEL CsF _n COMPOUND.....	67

EQUATION OF STATE MEASUREMENTS OF CESIUM FLUORIDE.....	70
CHAPTER 6: CONCLUSIONS.....	77
REFERENCES.....	79
CURRICULUM VITAE.....	83

List of Tables

Table 3.1: Table of 14 Bravais Lattices.....	22
Table 3.2: X-ray absorption edged and its corresponding electron orbital.....	30
Table 3.3: Selection rules for core electron transitions.....	32
Table 5.1: Summary the XANES modeling result for low and high pressure CsF phases.....	55
Table 5.2: Tabulated cell refinement data used for equation of state calculations.....	73

List of Figures

Figure 2.1: Raman spectra of decomposed KBF_4	5
Figure 2.2: X-ray diffraction patterns of decomposed KClO_4	6
Figure 2.3: Image of decomposed KClO_4 showing O_2 diffusion.....	7
Figure 2.4: Raman spectra of decomposed segregated mixture showing water formation.....	8
Figure 3.1: Visual representations of B1 and B2 phases of cesium fluoride.....	9
Figure 3.2: Visual representation of KBF_4	10
Figure 3.3: Images of diamond anvil cells used in experiments.....	11
Figure 3.4: Schematic of diamond anvil cell.....	12
Figure 3.5: Ruby fluorescence spectrum.....	13
Figure 3.6: Schematic of ruby fluorescence.....	14
Figure 3.7: Representation of electron cloud distortion by electric field.....	16
Figure 3.8: Diagram of electron transitions.....	17
Figure 3.9: Miller indices.....	23
Figure 3.10: Diagram of Braggs law.....	24
Figure 3.11: 2-D diffraction pattern and its integrated 1-D pattern.....	26
Figure 3.12: Diagram of mass absorption coefficient as a function of photon energy.....	29

Figure 3.13: Diagram of x-ray absorption.....	30
Figure 3.14: Typical x-ray absorption spectrum.....	31
Figure 3.15: Diagram of core electron transitions.....	33
Figure 3.16: Diagram showing difference between XANES and EXAFS.....	35
Figure 3.17: Diagram of EXAFS phenomenon.....	36
Figure 5.1: XANES spectra of mixture of CsF and KBF ₄	47
Figure 5.2: k-space and R-space transformations of data in figure 5.1.....	49
Figure 5.3: Image of irradiated mixture of CsF and KBF ₄	50
Figure 5.4: XAS spectra of pure CsF up to 68 Gpa.....	51
Figure 5.5: Models best fit to data in figure 5.4.....	52
Figure 5.6: k-space models best fit to data in figure 5.4.....	53
Figure 5.7: Calculated atomic distances.....	54
Figure 5.8: XAS spectra for second experiment.....	56
Figure 5.9: k-space and R-space transformations of data in figure 5.8.....	58
Figure 5.10: Backwards Fourier transforms of figure 5.9.....	59
Figure 5.11: XANES spectra for all pressures in second experiment.....	60
Figure 5.12: Model and experimental XAS data at 58 Gpa.....	61

Figure 5.13: Model and experimental XAS data at 64 GPa.....	62
Figure 5.14: Model of CsF ₂ plotted against experimental data at 64 GPa.....	63
Figure 5.15: Unit cells of CsF ₂ and CsF in B1 phase.....	64
Figure 5.16: XRD of irradiated mixture of CsF and KBF ₄ at 16 GPa.....	65
Figure 5.17: XRD of mixture at 64 GPa with patterns of potential compounds.....	65
Figure 5.18: XRD of mixture at 64 GPa with CsF ₂ pattern.....	66
Figure 5.19: Raman spectra of mixtures, pure CsF, and pure KBF ₄	67
Figure 5.20: DFT models of vibrational modes of CsF _n compounds.....	69
Figure 5.21: Decompression XRD experiment of pure CsF.....	70
Figure 5.22: XRD patterns of pure CsF up to 115 GPa.....	71
Figure 5.23: XRD patterns of pure CsF up to 115 GPa centered around 64 GPa.....	72
Figure 5.24: Normalized volumes as a function of pressure of pure CsF.....	74
Figure 5.25: Normalized pressure as a function of strain of pure CsF.....	75
Figure 5.26: EoS plot for B2 phase of pure CsF.....	76

List of Acronyms

APS – Advanced Photon Source

b.c.c. – Body Centered Cubic

CCD – Charge Coupled Device

DAC – Diamond Anvil Cell

EoS – Equation of State

EXAFS – Extended X-ray Absorption Fine Structure

f.c.c. – Face Centered Cubic

ICSD – Inorganic Crystal Structure Database

XAFS – X-ray Absorption Fine Structure

XANES – X-ray Absorption Near Edge Spectroscopy

XAS – X-ray Absorption Spectroscopy

XRD – X-ray Diffraction

Chapter 1

Introduction

Recent theoretical work predicted that cesium may undergo inner-shell bonding with fluorine under high pressure, forming higher oxidation species CsF_n ($n > 1$) [1]. Though inner shell electrons are usually inaccessible for bonding under ambient conditions, pressure can broaden and increase the energy of the 5p shell of cesium, allowing the electrons to react with a highly electronegative atom such as fluorine. Thus cesium, which has an electron configuration of $\text{Xe}[6s^1]$, possesses only one valence electron in the 6s shell to contribute to bonding (giving it a potential oxidation state of 1+). Under pressures greater than 5 GPa, it is predicted that the highly electronegative fluorine will begin to pull electrons out of the 5p shell causing the cesium and fluorine to undergo xenon like bonding [1].

The primary difficulty in synthesizing new stoichiometries of CsF_n is the challenge in working with fluorine due to its extremely reactive nature caused by its high electronegativity (4.0). Recent developments in *Useful Hard X-ray Induced Chemistry* offer a method to produce simple molecules for reaction *in situ* within a diamond anvil cell by decomposing relatively safe, inert, easy to work with solid crystalline powders by harnessing the highly ionizing and highly penetrating characteristics of hard x-rays. Using this technique, multiple species of simple molecules have been formed without catalysts, including H_2 , N_2 , O_2 , Cl_2 , and recently F_2 , all *in situ* within a diamond anvil cell [10-14]. We have also shown recently that polymeric CO and CO_2 can be formed when strontium oxalate is decomposed under pressure [16]. It has also been shown that controlled chemistry can be achieved at extreme pressures via the reaction of hydrogen, formed by the x-ray induced decomposition of ammonia borane, and oxygen formed

by the x-ray induced decomposition of potassium perchlorate, into water; all *in situ* within a diamond anvil cell at high pressure. OF_2 has also been formed by similar methods [14]. This experiment, combined with the successful formation of molecular fluorine via *Useful Hard X-ray Induced Chemistry* has given us a novel means to release F_2 and potentially perform fluorine chemistry under extreme conditions all *in situ*. The primary goal here is to produce a mixture of CsF and F_2 at high pressure, in order to potentially observe the formation of novel CsF_n compounds at pressures greater than 5 GPa.

Chapter 2

Background

2.1: Prediction of CsF_n (n>1) compounds

It has been shown that the electronic structure of cesium undergoes some very unique behavior under high pressure. Pure cesium metal undergoes a body centered cubic (b.c.c.) to face centered cubic (f.c.c.) structural transition above 2.5 GPa. After this phase transition, the unoccupied 5d level begins to become occupied with pressure by the elevation of the 6s and 5p electrons, allowing for the potential for higher oxidation states of the metal [18]. This effects is what lead to theoretical work by Miao showing that, under the presence of a highly electronegative ion, such as fluorine, the promoted 5p electrons in cesium can be utilized for bonding, forming CsF_n; thus, effectively increasing the formal oxidation state of cesium from +1 to +n (n = integer > 1) [1].

In Miao's work, Density Functional Theory (DFT) calculations using VASP (Vienna ab initio Simulation Package) were done in order to find the most energetically favorable structures of CsF_n compounds at different pressures. It was found that CsF could be reacted with F₂ in order to form higher stoichiometries of CsF_n via the following reaction [1]:



Miao's work theoretically predicted the existence of CsF_n in stoichiometric ratios as high as 1:6 at pressures up to 200 GPa. Using this work as a guide, and the newly developed tool of

useful hard x-ray induced chemistry, this thesis discusses our attempt at synthesizing these novel CsF_n compounds.

2.2: Useful hard X-ray induced chemistry

It is well known that when high energy X-rays are incident on a molecular system, x-ray induced decomposition can occur, especially in a covalently bonded system. It was a goal of our group to utilize this phenomenon in order to perform controlled chemistry *in situ* in a diamond anvil cell at extreme conditions. We believe the process involved in driving x-ray induced chemistry is based on inner shell absorption of the high energy x-rays. When an inner shell electron either gets ejected as a photoelectron or gets excited into a higher vacant shell; in either occurrence, a “hole” is formed where the exited electron was. The inner shell “wants” to be filled, so a higher shell electron will fall into that hole, this electron typically comes from the outer unfilled shell, which is the electron used for bonding. When this electron is being shared in a bond, it will get stolen away from this bond, effectively destabilizing the bond. This destabilization leads to the bond breaking and the atoms being ejected as highly excited radicals. These radicals exist for a short period of time until they relax and bond with a nearest neighbor, preventing healing of the original molecule, and forming completely new molecular species.

In the instance of the following reaction:



The Cl-O bonds in the ClO₃⁻ anion are broken via the process discussed above; the oxygen radicals are formed in a highly energized state, preventing them from re-bonding with the Cl atom right away. This allows a highly stable ionic salt, KCl, to form, and creates the environment for the O₂ molecules to form. It should also be noted that when these molecules form, they

eventually do so in the ordered solid crystalline structure that is most energetically favorable at the pressures the molecules are formed.

There are some decomposition reactions that are not yet fully understood. The decomposition of potassium tetraborofluorate (KBF_4) is one such reaction. We know that F_2 is formed via the decomposition of KBF_4 via Raman spectroscopy [15]

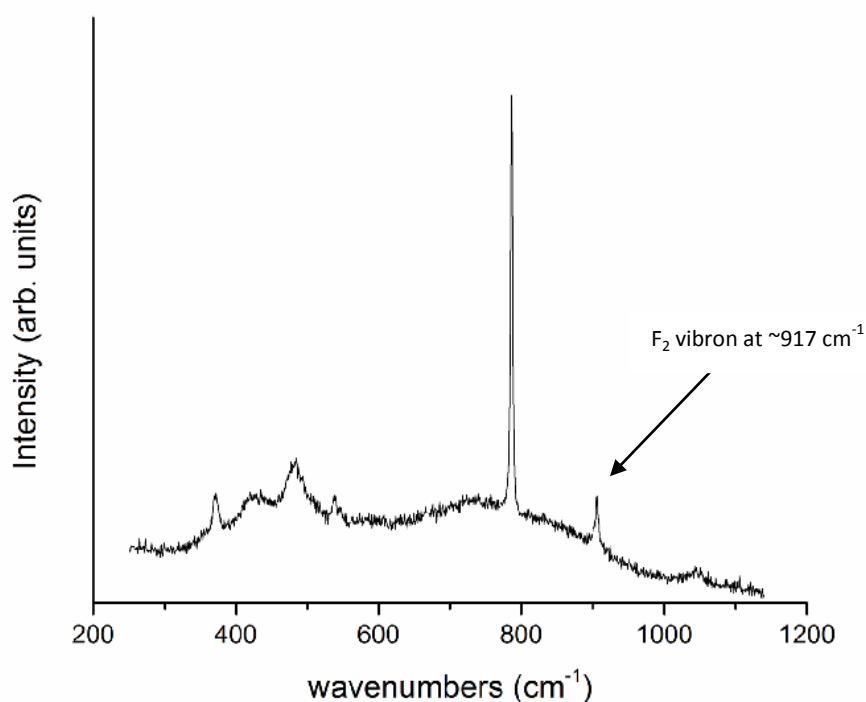
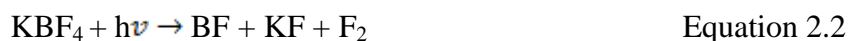


Figure 2.1: Raman spectrum of decomposed KBF_4 showing evidence of molecular fluorine via the F_2 vibron, located at $\sim 917 \text{ cm}^{-1}$ [15].

But the stoichiometry is not well understood. There are many different polymers of BF that may possibly form, such as BF_3 , B_2F_4 , or $\text{B}_{10}\text{F}_{14}$, but these compounds will not allow for the formation F_2 stoichiometrically. Because of this, the most likely reaction is:



Fluoroborylene (BF) is an unstable gas that can be synthesized by reacting BF_3 with a boron rod at 2000 °C, it can be condensed into a liquid at 77 K [20]. Though it is unstable at ambient pressures, it has never been studied with pressure, so its quasistable existence under the high pressure conditions in conjunction with *Useful Hard X-ray Induced Chemistry*, may be possible.

During our studies of the O_2 formation via the x-ray decomposition of KClO_3 and KClO_4 , we discovered that oxygen was highly mobile, and though formed as a solid crystal shown via x-ray diffraction, we also found evidence of the diffusion of molecular oxygen [10, 21].

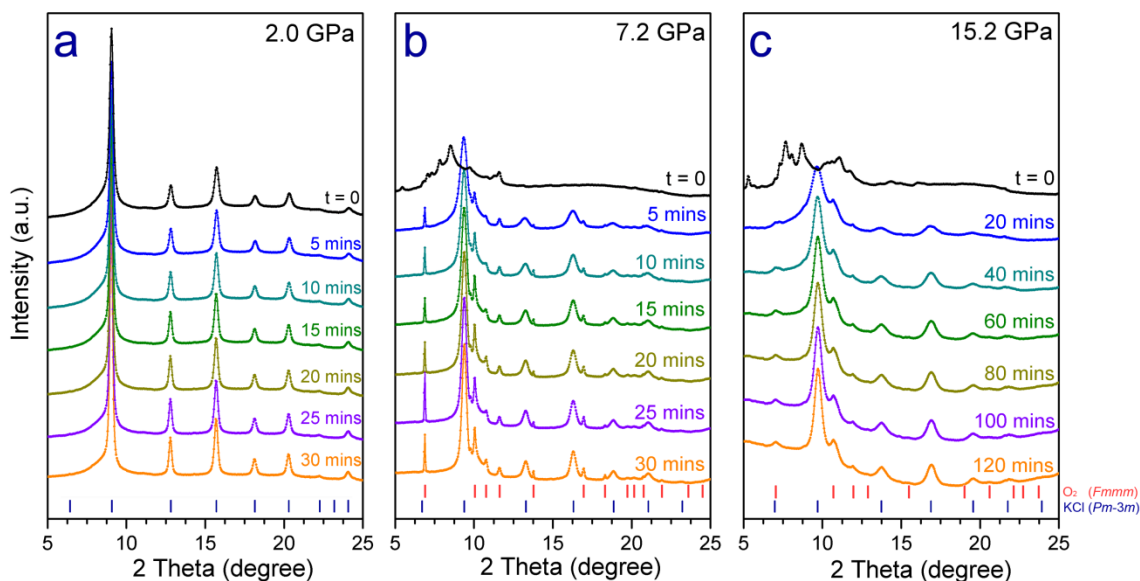


Figure 2.2: X-ray diffraction of decomposed KClO_4 showing the formation of both KCl and solid O_2 [21].

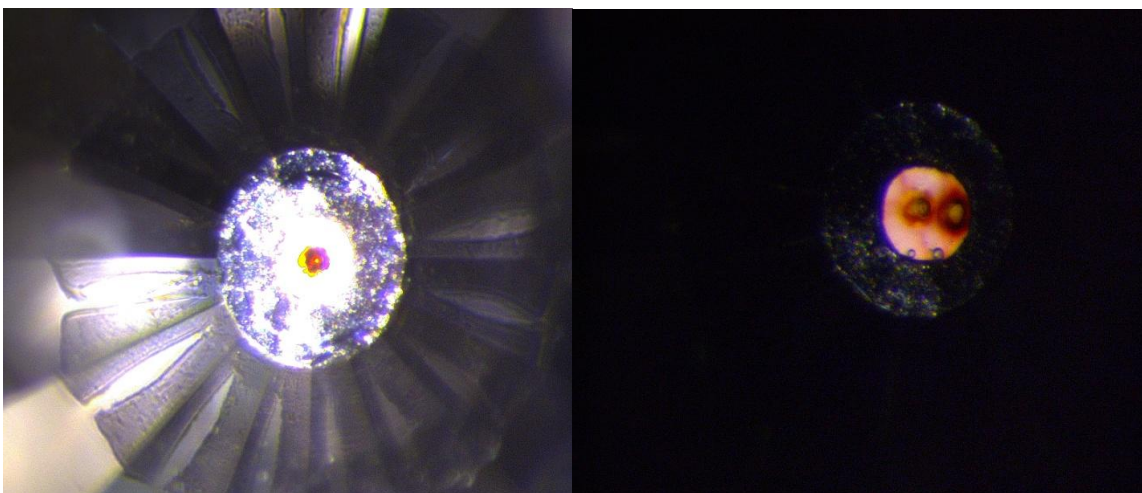


Figure 2.3: Decomposed KClO_4 showing solid oxygen diffused throughout the sample chamber [10].

Though the irradiated KClO_4 eventually formed into the solid phase of oxygen, it exists in some excited state long enough to diffuse throughout the sample chamber, even under pressures as high as 9 GPa. After making this discovery, we sought to determine if this behavior could be utilized in order to perform novel chemistry at high pressures. We knew H_2 could be formed via the x-ray decomposition of ammonia borane (NH_3BH_3), a special “keyhole” gasket was prepared in which we laser drilled a stainless steel gasket indented with 300 micron diamonds with two overlapping holes. In one hole we loaded NH_3BH_3 , and in the other hole KClO_4 was loaded. We pressurized the cell to 5 GPa and proceeded to irradiate the KClO_4 , verifying the formation of O_2 throughout the cell via Raman spectroscopy. Next we irradiated the NH_3BH_3 and verified the presence of H_2 via Raman Spectroscopy, an interesting thing to note is that, though the oxygen diffused throughout the sample chamber, the hydrogen remained localized to the irradiation area (see figure below). We then verified the presence of the O-H stretch at approximately 3100 cm^{-1} and 3500 cm^{-1} via Raman spectroscopy, this reaction only occurred in the regions of irradiated NH_3BH_3 [12].

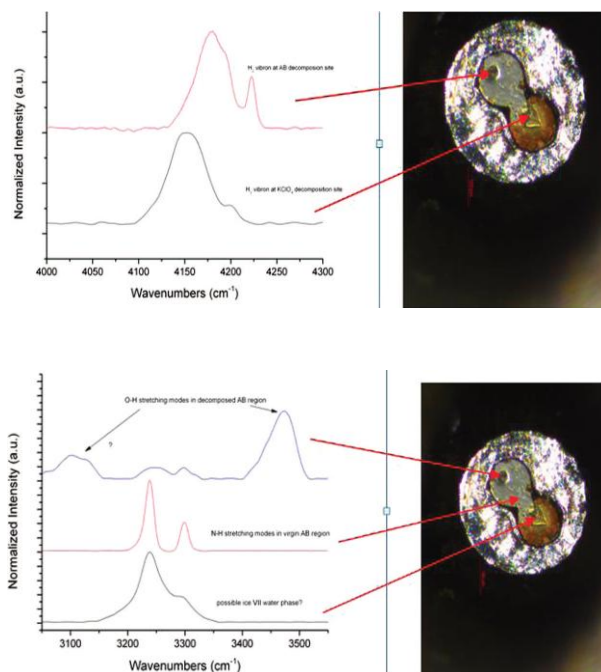


Figure 2.4: Raman spectra of decomposed segregated mixture of KClO_4 and NH_3BH_3 showing formation of H_2 (top) and H_2O (bottom) [12].

This was the first demonstration of novel chemistry, driven purely by x-ray decomposition under high pressures, that we know of [12].

Once we had successfully demonstrated that we could produce fluorine via hard x-ray induced chemistry, along with successfully synthesizing water useful hard x-ray induced chemistry at high pressures, we felt it prudent to attempt new novel synthetic routes of chemistry. It was at this point that recent theoretical work was brought to our attention discussing the potential formation of higher stoichiometries of CsF via the reaction of cesium and fluorine under pressures greater than 5 GPa. We felt that we could use our technique of useful hard x-ray induced chemistry in order to attempt to synthesize these novel cesium fluoride compounds.

Chapter 3

General Theory

3.1: Cesium Fluoride

Cesium fluoride (CsF) is a highly ionic salt that has many uses in organic chemistry, spectroscopy, and nuclear medicine. In organic chemistry it is used as a source of fluorine ions for the removal of silicon groups due to the strong Si-F bond [22]. In nuclear medicine it is used as a scintillator in positron emission tomography due to its fast response time, allowing better resolution in time of flight measurements [23]. As it is very hygroscopic, it must be handled under an inert dry atmosphere, and it is extremely toxic due to formation of hydrofluoric acid when reacting with water. CsF has a well studied phase transition, going from the B1 phase, which is an $fm\bar{3}m$ NaCl structure, to the B2 phase, which is a $pm\bar{3}m$ CsCl structure, at approximately 4.8 GPa [38].

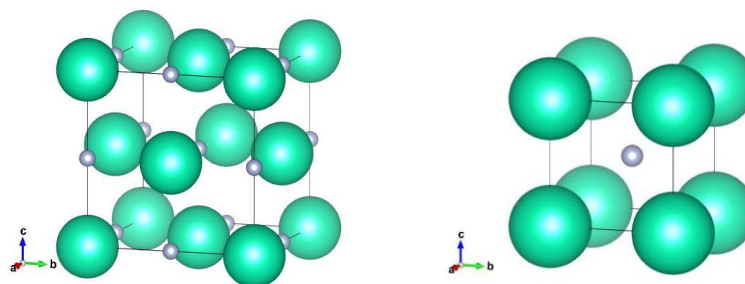


Figure 3.1: Visual representations of the B1 phase (left) and B2 phase (right) of cesium fluoride created in Powdercell®.

3.2: Potassium tetrafluoroborate

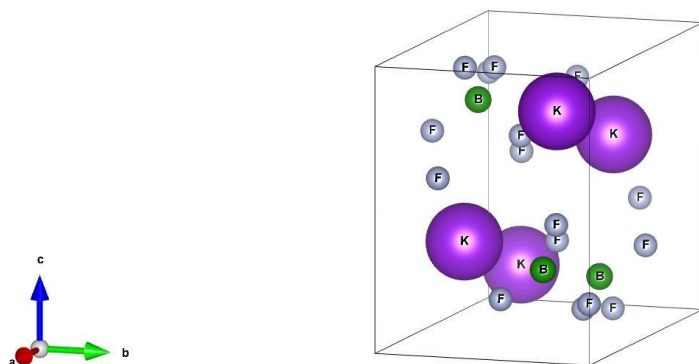


Figure 3.2: Visual representation of potassium tetrafluoroborate (KBF₄) created in Powdercell®.

3.3: Diamond Anvil Cells

As pressure is force applied per unit area (N/m^2), there are only two ways to apply a large amount of pressure on a system: apply a large amount of force across a surface, or apply a relatively small amount of force across an extremely small area. As applying a large amount of force requires a lot of work, it is much easier to apply a relatively small amount of force across a microscopic area; this is exactly how a Diamond Anvil Cell (DAC) works. There are many different types of DAC's, but they all follow the same principle. Two diamonds are mounted on seats with a small hole drilled through the center. These seats are set in a large vessel that works like a piston in a cylinder which allows application of pressure perpendicularly to the diamond face.



Figure 3.3: Images of panoramic- (top left), Mao-Bell- (top right), and symmetric-style (bottom) diamond anvil cells.

The tips of the diamonds are cut down and polished flat so that a small culet is created. This culet size ranges from as small as 20 μm to as large as 1 mm in diameter, all depending on the desired terminal pressure. A series of screws are aligned to apply force symmetrically as the diamonds are brought together; spring washers are used to ensure that the pressure is applied evenly.

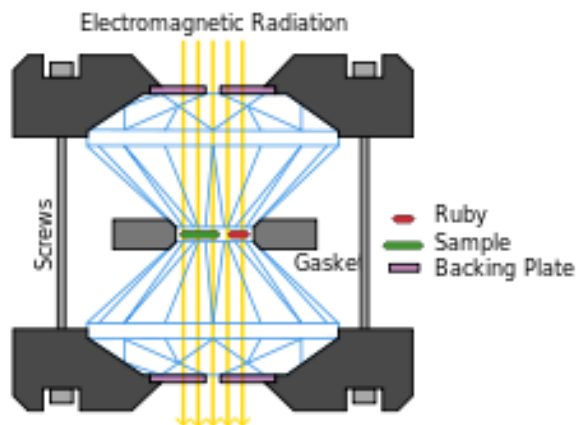


Figure 3.4: Schematic of a typical diamond anvil cell [24].

Though diamonds can undergo extremely high levels of compressive stress, they are very weak to any type of shear strain. They are also very likely to damage each other if they come into direct contact, so for these reasons, a soft metal gasket is placed in between the diamonds to prevent the diamonds from touching, as well as to confine and pressurize the sample. This gasket is pre-indented to a width of typically 10 - 50 μm , and a hole no greater than one half of the diameter of the diamond culet is drilled into the center of the indentation. The initial starting thickness and hole size are dependent upon the maximum pressure desired. For higher pressures, the gasket starting thickness should be thinner, and the hole diameter should be closer to one third of the culet size. The sample is placed in this hole, along with a small ruby or other pressure calibrant. If pressures greater than 50 GPa are desired, and x-rays are going to be used for an experiment, a metal such as gold or tungsten can be used as a pressure calibrant by measuring the cell volume via x-ray diffraction, and fitting this volume to a known equation of state of that particular metal.

3.4: Ruby Fluorescence

The R1 fluorescence peak is used to gauge how much pressure is applied to the sample due to a systematic shift to the R1 fluorescence peak that has been measured and calibrated. This calculation has been well explored and verified, and shown to have the following relationship [8]:

$$P = \frac{1904}{9.827} * \left[\left(1 + \frac{\Delta\lambda}{\lambda_0} \right)^{9.827} - 1 \right] \quad \text{Equation 3.1}$$

Where $\Delta\lambda$ is the measured wavelength, λ_0 is the ruby wavelength at ambient conditions, and P is the hydrostatic pressure applied at the ruby.

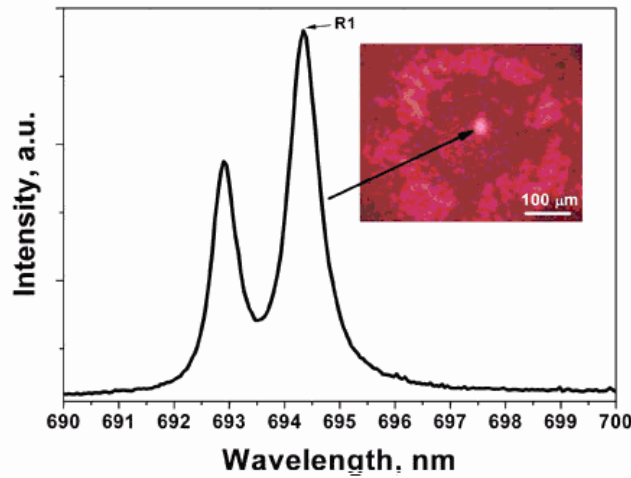


Figure 3.5: Example of ruby fluorescence spectrum [7].

The ruby fluorescence spectrum is a result of Cr_3^+ doping of an Al_2O_3 crystal. The 3d electrons in the Cr_3^+ ions are excited from their ground state into an excited electronic state. The electrons then de-excite vibrationally into a lower energy metastable state. The electrons then de-

excite further back to their ground state emitting a photon of a wavelength equal to the energy difference.

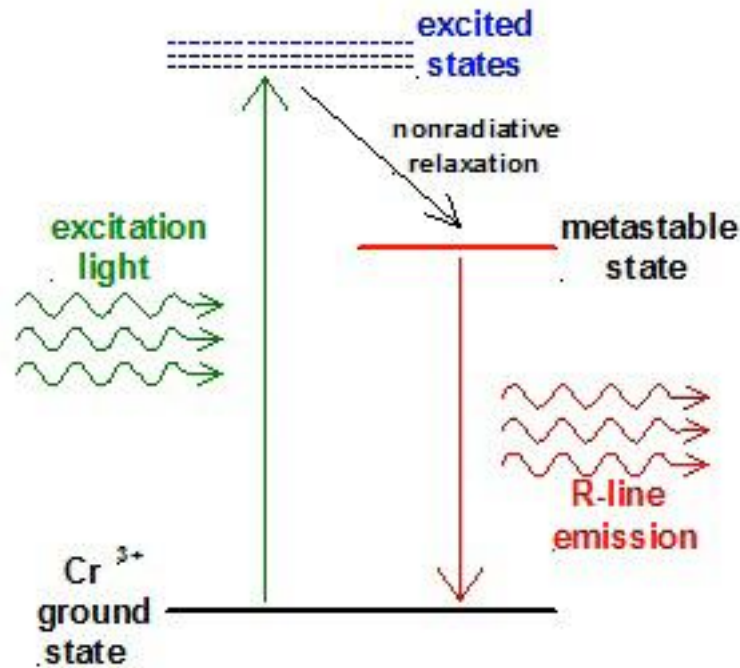


Figure 3.6: Schematic representation of ruby fluorescence spectrum [25].

There is a splitting of the fluorescence lines due to interactions of the Cr_3^+ ion with the Al_2O_3 crystal lattice via the electrostatic crystalline field. The lower energy fluorescence peak is called the R1 fluorescence peak, and has a typical starting wavelength of 694.22 nm, though there are differences between rubies based on the starting Cr_3^+ concentration [26]. It is the R1 fluorescence line that has been well studied and calibrated, though the R2 line follows the same behavior as the R1 line. The shift of the ruby peak is a direct result of the decreasing interatomic distances within the Al_2O_3 lattice. As the interatomic distances reduce with pressure, the bonds stiffen, requiring more energy to be taken from the excited electrons during relaxation to the metastable state.

3.5: Raman

Raman spectroscopy is a very powerful spectroscopic technique used to observe vibrational, rotational, and phonon, or intra-molecular, modes in a molecular system [2]. It relies on inelastic scattering of photons from a monochromatic light source, usually from a laser in the visible, near infrared, or near ultraviolet range. A photon couples with the electrons in a bond causing different intra- and inter-molecular vibrations, and the shift in energy gives information about the bonds, electronic environment, and atomic species that a specific molecular system has. The energy of the photon can be scattered elastically, in which the energy of the photon does not change during the scattering process, or inelastically. When the photon is scattered inelastically, its energy can be changed via two different processes; it can either be stokes shifted, in which energy is taken from the photon during the scattering process, or anti-stokes shifted, in which energy is actually given to the scattered photon.

The majority of the photons emitted by the sample are elastically scattered, so they have a wavelength close to that of the excitation source, this is called elastic Rayleigh scattering. Raman scattering is typically very weak, especially relative to the elastically scattered Rayleigh light, and as a result the primary difficulty of Raman spectroscopy is separating the weak inelastically scattered light from the intense Rayleigh scattered laser light [2].

The Raman effect occurs when light interacts with the electron clouds associated with molecular bonds. An incident photon has an electric field that can couple with the charge distribution of a molecular bond. The electric field of the photon causes a deformation of the electron cloud distribution, via the polarization tensor; the magnitude of this deformation is proportional to the field strength of the photon. The proportionality constant α , known as the

polarizability constant, determines exactly how much the bond will be deformed. Thus, the dipole moment of the bond changes in response to coupling with the photon, creating a new induced dipole moment. This new dipole moment can be described by the equation:

$$\vec{\mu}_{induced} = \vec{\alpha} \cdot \vec{E} = \alpha E_0 \cos(\omega_0 t) \quad \text{Equation 3.2}$$

This induced dipole moment will have a torque applied to it, causing the bonds to tend to orient with the polarization of the inbound photons polarization axis.

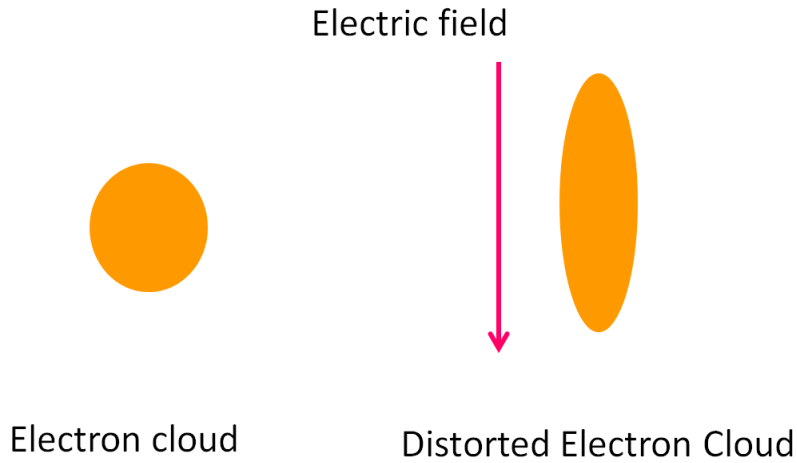


Figure 3.7: Image showing how an electron cloud can be distorted by an external electric field [2].

During this distortion, electrons are excited into a virtual state; when the bond relaxes, the electrons return to either their ground state configuration (Rayleigh scattering), or an excited ground state (Stokes shifting). This transition is governed by the selection rules of the bond, shown by the following function:

$$\langle \psi_f | \vec{\mu}_{induced} | \psi_i \rangle = \langle \psi_f | \vec{\alpha} \cdot \vec{E} | \psi_i \rangle \quad \text{Equation 3.3}$$

where $\vec{\alpha}$ is the polarization tensor, and is a tensor of rank 2, \vec{E} is the electric field vector, ψ_i is the wave function of the bond in its initial state, and ψ_f is the wave function of the bond in its final state. In matrix form, Equation 1 can be represented by:

$$\begin{pmatrix} \mu_{induced,x} \\ \mu_{induced,y} \\ \mu_{induced,z} \end{pmatrix} = \begin{pmatrix} \alpha_{xx} & \alpha_{xy} & \alpha_{xz} \\ \alpha_{yx} & \alpha_{yy} & \alpha_{yz} \\ \alpha_{zx} & \alpha_{zy} & \alpha_{zz} \end{pmatrix} \begin{pmatrix} E_x \\ E_y \\ E_z \end{pmatrix} \quad \text{Equation 3.4}$$

In normal Raman scattering, the polarization tensor is symmetric, so

$\alpha_{xy} = \alpha_{yx}, \alpha_{zy} = \alpha_{yz}, \alpha_{zx} = \alpha_{xz}$. Because of the symmetry of Equation 3.4, transitions are forbidden if it is equal to zero. In other words, a transition is only Raman active if Equation 3.4 is even.

As stated earlier, when a photon couples with a molecular bond, the electrons in the bond are excited from its initial state to a virtual state, then relax to an excited ground state, which is called Stokes shifting. It is also possible for the electrons in the bond to have started in the excited ground state, and then relax back to the ground state, this is called anti-Stokes shifting. Figure 3.8 is a graphical representation of Rayleigh scattering, Stokes shifting, and anti-Stokes shifting.

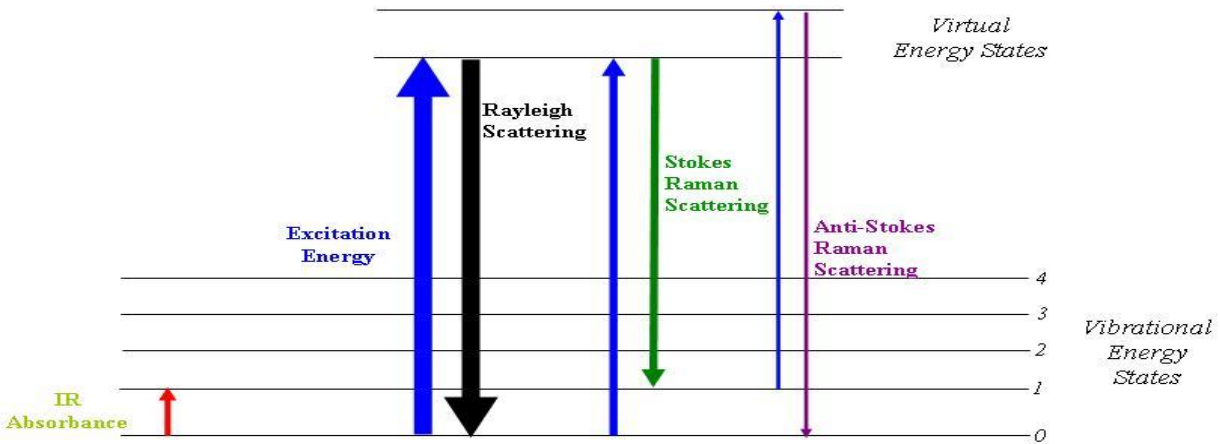


Figure 3.8: Diagram of electron transitions that occur when a bond couples with a photon [3].

It should be noted that these virtual states are lower energy than electronic transitions, which are the basis of fluorescence. Because the ability to perturb the local electron cloud of a molecule depends on the relative location of the individual atoms, it can be seen in Equation 3.4 that the polarizability is dependent on the instantaneous position of the atoms [4]. For any molecular bond, the individual atoms are confined to specific degrees of freedom, in which the vibrational energy levels are quantized in a manner similar to that of electronic transitions. These quantized energy levels are given by the following expression [3]:

$$E_{vib} = \left(j + \frac{1}{2}\right) h\nu_{vib} \quad \text{Equation 3.5}$$

Where j is the vibrational quantum number ($j = 0, 1, 2, 3, \dots$), and ν_{vib} is the frequency of the vibrational mode. The physical displacement, dX , of the atoms about their equilibrium positions during a particular vibrational mode can be expressed as [4]:

$$dX = X_0 \cos(\omega_{vib} t) \quad \text{Equation 3.6}$$

Where X_0 is the maximum displacement about the equilibrium position. For a typical molecule, the maximum displacement is relatively very small compared to the bond length. Since dX is small relative to the bond lengths, α can be expanded as a Taylor series, giving [3]:

$$\alpha = \alpha_0 + \frac{\partial \alpha}{\partial X} dX + \dots \quad \text{Equation 3.7}$$

Where α_0 is the polarizability of the molecular bond in its equilibrium state. Combining Equation 3.6 and Equation 3.7 gives:

$$\alpha = \alpha_0 + \frac{\partial \alpha}{\partial X} X_0 \cos(\omega_{vib} t) \quad \text{Equation 3.8}$$

Combining Equation 3.8 with Equation 3.2 gives:

$$\vec{\mu}_{induced} = \alpha_0 E_0 \cos(\omega_0 t) + \frac{\partial \alpha}{\partial X} X_0 E_0 \cos(\omega_0 t) \cos(\omega_{vib} t) \quad \text{Equation 3.9}$$

This simplifies into [4]:

$$\vec{\mu}_{induced} = \alpha_0 E_0 \cos(\omega_0 t) + \frac{\partial \alpha}{\partial X} X_0 E_0 \cos\{(\omega_0 - \omega_{vib})t\} + \cos\{(\omega_0 + \omega_{vib})t\} \quad \text{Equation 3.10}$$

Equation 3.10 gives the classical relationship between the induced dipole moment, the polarization tensor and the vibrational modes of the molecule. It can also be seen from Equation 3.10 that the polarization tensor must change in order for there to be any form of inelastic scattering. The first term is for Rayleigh scattered photons, the second term is for Stokes shifted photons, and the final term is for anti-Stokes shifted photons. Equation 3.10 can also be expanded higher to describe higher order Raman scattering, but these events are typically very weak and can usually be ignored.

The Raman scattering intensity is dependent upon the amount that the polarization of a bond and the spectral modes are determined by the rotational and vibrational states of the sample. This dependence on the polarization differs from Infrared spectroscopy where the interaction between the molecule and light is determined by the dipole moment. IR spectroscopy has the advantage over Raman that it is not plagued by sample fluorescence due to the photon energy not being high enough to excite electronic transitions. Thus, combining IR and Raman spectroscopy can yield a more complete picture of the molecule being studied.

Raman shifts are typically expressed in wavenumbers, which represents the number of waves that exist within 1 cm, and have units of inverse length. In order to convert between wavelength and wavenumbers of the Raman spectrum, the following formula can be used:

$$\Delta\nu = \left(\frac{1}{\lambda_0} - \frac{1}{\lambda} \right) \quad \text{Equation 3.11}$$

Where $\Delta\nu$ is the Raman shift expressed in wavenumbers, λ_0 is the excitation wavelength, and λ_1 is either the Stokes or anti-Stokes shifted photon wavelength. Most commonly, the units chosen for expressing wavenumber in Raman spectra is inverse centimeters (cm^{-1}). Since wavelength is often expressed in units of nanometers (nm), Equation 10 can scale for this unit conversion, giving:

$$\Delta\nu(\text{cm}^{-1}) = \left(\frac{1}{\lambda_0(\text{nm})} - \frac{1}{\lambda(\text{nm})} \right) \times 10^7 \quad \text{Equation 3.12}$$

Raman spectroscopy is a commonly used technique in chemical analysis since vibrational information is specific to the chemical bonds and the symmetry of molecules. Because of this, it provides a fingerprint by which a molecule can be identified. One example of this would be the vibrational frequencies of SiO , Si_2O_2 , and Si_3O_3 . These different frequencies were identified and assigned based on normal coordinate analyses using infrared and Raman spectra [4]. Raman spectroscopy can also be used to characterize materials, measure temperature, and find the preferred orientation of a sample. As with single molecules, a given solid material has characteristic phonon modes that can help to identify it. Raman is also used to identify changes to crystal lattices under high pressures and temperatures, and can also be used to observe phase transitions in materials.

3.6: Crystal Structure of material

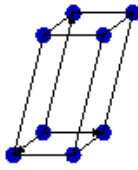
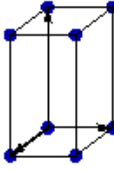
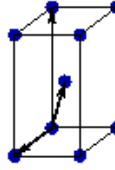
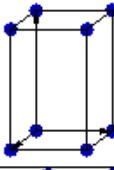
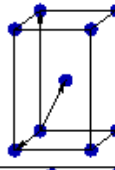
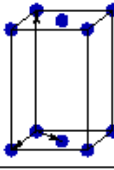
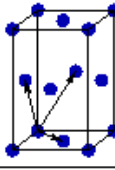
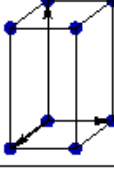
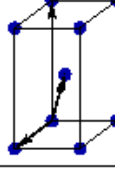

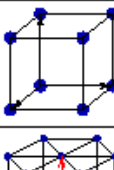
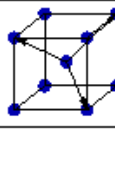
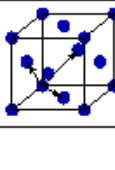
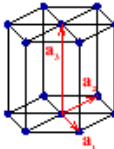
In nature, most solids adopt a crystalline structure when in equilibrium which can be described by something called a Bravais lattice. A Bravais lattice is an array of discrete points that extends out infinitely in three dimensional space. These points can be defined by a set of translation operations determined by the vector [27]:

$$\mathbf{R} = n_1 \mathbf{a}_1 + n_2 \mathbf{a}_2 + n_3 \mathbf{a}_3 \quad \text{Equation 3.13}$$

Where n is any integer value and ' \mathbf{a} ' is a set of primitive basis vectors of the lattice, the combination of which can describe the unique position of any point within the lattice. The infinite nature of the Bravais lattice means that for any choice of the vector \mathbf{R} the lattice appears exactly the same when viewed from any different point within the array, separated by the translation of one unit cell.

The Bravais lattice can be categorized into 7 different crystal systems based on point group symmetry, or symmetry that leaves a particular point fixed (non-translational) in a unit cell. Each crystal symmetry can be described by the three vectors: a , b , and c , which are the relative lengths of the edges in each direction of a unit cell and the angles in between them: α , β , and γ . Those seven crystal systems can be broken down into 14 crystal systems based on how the lattice is centered on the unit cell. Those 14 crystal systems are as follows:

Table 3.1: Table of 14 Bravais Lattices [28].

Bravais lattice	Parameters	Simple (P)	Volume centered (I)	Base centered (C)	Face centered (F)
Triclinic	$a_1 \neq a_2 \neq a_3$ $\alpha_{12} \neq \alpha_{23} \neq \alpha_{31}$				
Monoclinic	$a_1 \neq a_2 \neq a_3$ $\alpha_{23} = \alpha_{31} = 90^\circ$ $\alpha_{12} \neq 90^\circ$				
Orthorhombic	$a_1 \neq a_2 \neq a_3$ $\alpha_{12} = \alpha_{23} = \alpha_{31} = 90^\circ$				
Tetragonal	$a_1 = a_2 \neq a_3$ $\alpha_{12} = \alpha_{23} = \alpha_{31} = 90^\circ$				
Trigonal	$a_1 = a_2 = a_3$ $\alpha_{12} = \alpha_{23} = \alpha_{31} < 120^\circ$				
Cubic	$a_1 = a_2 = a_3$ $\alpha_{12} = \alpha_{23} = \alpha_{31} = 90^\circ$				
Hexagonal	$a_1 = a_2 \neq a_3$ $\alpha_{12} = 120^\circ$ $\alpha_{23} = \alpha_{31} = 90^\circ$				

When the rotational, translational, inversion, and reflection symmetry operations are included, the 14 crystal systems can be broken down even further into 230 unique space groups.

Each space group can be described by the unique symmetry operations that can describe a given structure, and each space group can describe the unique positions of the atoms within a unit cell.

3.7: X-ray Diffraction

Based on the properties of the Bravais lattice, atoms will align themselves in infinite arrays determined by the atomic species and bond lengths. There are different planes that can be formed by these arrays of atoms, which are called Miller indices and are denoted by the n_1 , n_2 , and n_3 in Equation 16. They are better known as the indices h , k , and l , and they represent the vectors of each direction of the crystal. The different Miller indices can take many forms, the following diagram showing a few examples:

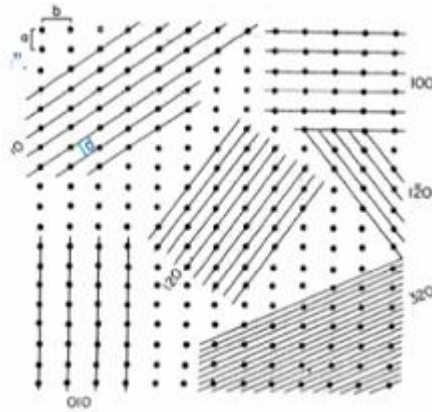


Figure 3.9: Two dimensional representation of Miller indices [32].

Where a and b are the unit cell parameters, and d is the distance in between atomic plains, the length of which is on the order of an angstrom (\AA).

X-rays are ideal for probing the inter-atomic spacings (d spacing) in a crystal lattice due to the fact that their wavelength is on order of the distance between atoms in a bond. When X-

rays are incident upon a specific plain, they have a probability of being reflected off of that plane. When X-rays are reflected off of given planes in a crystal lattice, they can either interfere with each other constructively, or destructively. This behavior is the basis behind x-ray diffraction and can be described by Bragg's law:

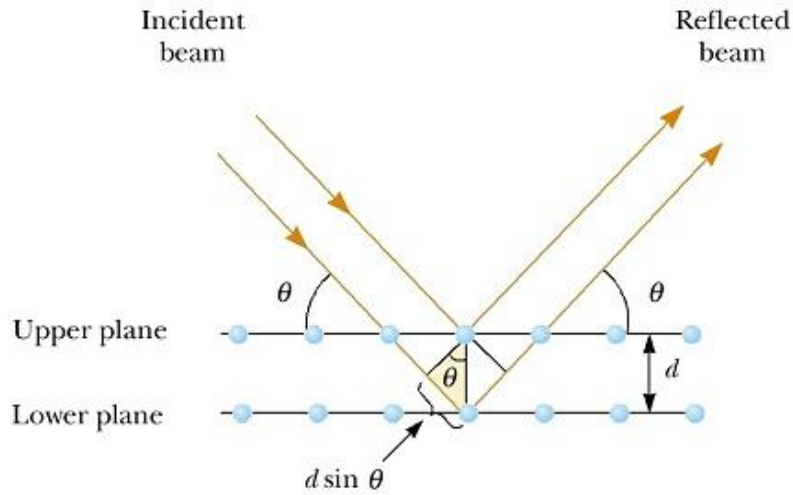


Figure 3.10: Visual representation of Bragg's Law [32].

Where θ is the angle of incidence and reflection and d is the distance in between reflection planes. Whether or not the reflected x-rays will interfere constructively is determined by the following relationship:

$$n\lambda = 2d\sin(\theta) \quad \text{Equation 3.14}$$

The probability that an x-ray will be reflected off of a given plane is determined by something called the structure factor, F_{hkl} [32]:

$$F_{hkl} = \sum_{n=1}^N f_n e^{2\pi i(hx_i + ky_i + lz_i)} \quad \text{Equation 3.15}$$

Here, f_n is known as the atomic form factor and describes how a single atom will scatter a given x-ray photon, x, y, and z describe the atomic positions, and h, k, and l describe which reflection plane will be expected. The intensity of the reflected x-rays are proportional to the square of the magnitude of the structure factor, or:

$$I \approx |F_{hkl}|^2 \quad \text{Equation 3.16}$$

The relationship between the d spacing and the unit cell parameters is as follows:

$$d_{hkl} = \sqrt{\frac{a^2}{h^2} + \frac{b^2}{k^2} + \frac{c^2}{l^2}} \quad \text{Equation 3.17}$$

In a synchrotron x-ray diffraction experiment, a broad spectrum of x-rays (2-100 KeV) is generated by electrons that have been accelerated to near the speed of light. There is a primary storage ring that is composed of straight sections and curved sections, along the curved section bending magnets steer the electrons to the next straight section, creating x-rays via Bremsstrahlung (breaking) radiation. There are also magnetic “wigglers” installed in the straight sections that generate x-rays via Bremsstrahlung radiation. These x-rays are directed into a beamline via special mirrors, and specially designed crystal monochromators are used to select out specific wavelengths via Equation 17 [33]. These x-rays are then focused onto a sample and the diffracted x-rays are collected by a specialized detector. This generates a 2-dimensional pattern that must then be integrated into a 1-dimensional diffraction pattern via specialized software such as Fit2d® or Dioptas®.

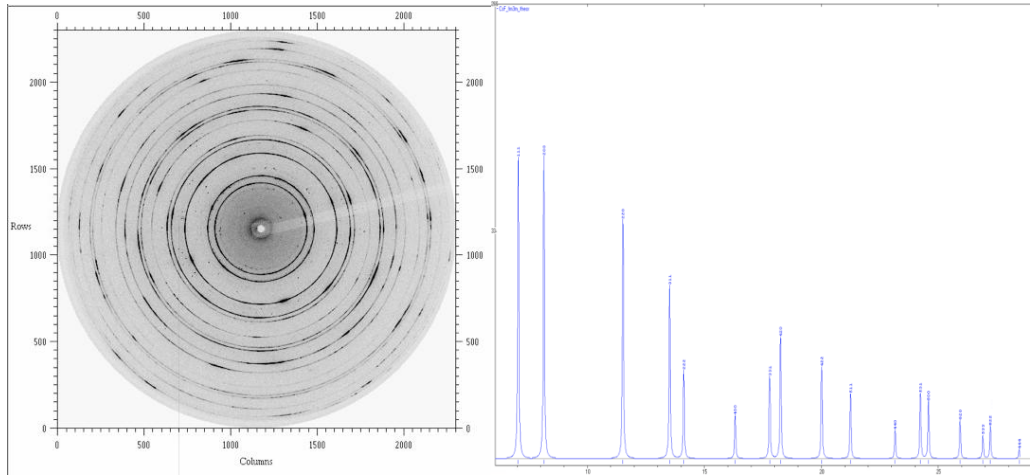


Figure 3.11: Two dimensional diffraction pattern of CsF (left) and an integrated one dimensional diffraction pattern of CsF (right) integrated via Fit2d®.

By fitting the peaks in the one dimensional diffraction pattern with a pseudo-Voigt function, and comparing those peaks to known structural data, the unit cell parameters a , b , and c can be determined. From these unit cell parameters, and information about the crystal system, the unit cell volume can be calculated. Unique atomic positions and percent composition can also be extrapolated through this type of refinement.

3.8: Equation of State

The isothermal equation of state (EoS) of a system is a description of how the volume of a solid material changes with an applied pressure at a constant temperature. How the volume of a solid changes with pressure can be described by the bulk modulus of that material, which is defined as:

$$K_0 = -V_0 \frac{\partial P}{\partial V} \quad \text{Equation 3.18}$$

Here, K_0 and V_0 are the bulk modulus and volume at ambient pressure respectively. There are multiple equation of states that are used, which depend on the system being studied. For the

purpose of this thesis, I will only focus on the Murnaghan and the Birch-Murnaghan equations of state.

The first isothermal equation of state that is widely used is known as the Murnaghan EoS. This equation of state is based off of the assumption that the bulk modulus of a material varies linearly with pressure, giving a P-V relationship of:

$$P = \frac{K_0}{K_0'} \left\{ \left(\frac{V_0}{V} \right)^{K_0'} - 1 \right\} \quad \text{Equation 3.19}$$

The Murnaghan equation of state has been shown to accurately represent experimental data, and give correct values for ambient pressure bulk modulus for compressions of up to 10%, or V/V_0 of 0.9 [29].

For compressions that are greater than 10%, a more sophisticated relationship must be made. The Birch-Murnaghan equation of state is one such relationship which utilizes a combination of a Taylor series expansion of finite strain, f_E :

$$f_E = \frac{1}{2} \left[\left(\frac{V_0}{V} \right)^{\frac{2}{3}} - 1 \right] \quad \text{Equation 3.20}$$

and the Murnaghan EoS [28]. This expansion taken to the fourth order yields the following equation of state:

$$P = 3K_0 f_E (1 + 2f_E)^{5/2} \left[1 + \frac{3}{2}(K' - 4)f_E + \frac{3}{2} \left[K_0 K'' + (K' - 4)(K' - 3) + \frac{35}{9} \right] f_E^2 \right] \quad \text{Equation 3.21}$$

This equation can be expressed as a function of normalized pressure, F , which is defined as:

$$F = \frac{P}{3f_E(1+2f_E)^{5/2}} \quad \text{Equation 3.22}$$

Combining Equations 3.21 and 3.22 yeilds:

$$F = K_0 \left\{ 1 + \frac{3}{2}(K' - 4)f_E + \frac{3}{2} \left[K_0 K'' + (K' - 4)(K' - 3) + \frac{35}{9} \right] f_E^2 \right\} \quad \text{Equation 3.23}$$

In order to determine which order of the Birch-Murnaghan EoS to use, data must be plotted in the form of normalized pressure, F , as a function of natural strain f_E . If data takes the form of a horizontal line, then a 2nd order Birch-Murnaghan must be used, implying that K' is set to 4, and K'' is set to -0.1886. Doing so sets the coefficients of f_E and f_E^2 to zero, and the equation of state only depends on P , K_0 , V , and V_0 . If the F versus f plot takes a linear slope, then a third order Birch-Murnaghan must be used, meaning that K'' is set to -0.1886 and the EoS depends on P , K_0 , V , V_0 , and K' . If the F versus f plot takes a parabolic form, then the full 4th order Birch-Murnaghan must be used [29].

3.9: X-ray Absorption Spectroscopy

X-ray Absorption Spectroscopy (XAS) is a spectroscopic technique used to probe the electronic environment as well as the local structure around a select atom. Electrons are bound to the nucleus of an element in very specific energy states, otherwise known as orbitals. The atomic number (Z) determines the number of electrons that can be bound to a specific neutral atom. In the case of cesium with a Z of 55, there are 55 electrons that exist in specific orbitals or shells that are designated by its principle quantum numbers $n = 1, 2, 3, 4$, and subshells designated by its azimuthal quantum number $l = 0, 1, 2, 3, 4$. The principle quantum numbers can also designated by characteristic x-rays, K, L, M, and N. This is the notation that will be utilized for the rest of this thesis. The azimuthal quantum numbers break down the electron subshell configuration into the more commonly known s,p,d,and f subshells.

XAS is a phenomenon based around Beer's law of absorption:

$$I = I_0 e^{-\mu t} \quad \text{Equation 3.24}$$

Here, I_0 is the x-ray flux before passing through the sample, I is the x-ray flux after passing through the sample, μ is known as the mass absorption coefficient, and t is the thickness of the sample. The variable μ is explained by the following expression [30]:

$$\mu \approx \frac{\rho Z^4}{AE^3} \quad \text{Equation 3.25}$$

Where ρ is the density of the element, Z is the atomic number, A is the atomic mass, and E is the exciting photon energy. Thus, as is evident from the previous expression, the absorption coefficient is a function of only energy for a given element [31]. The absorption coefficient is a continuous function of energy except for discontinuities at specific resonance points at which the energy of the excitation photon is equal to that of the binding energy of that shell. This can be seen in the following diagram of the absorption coefficient as a function of energy for cesium.

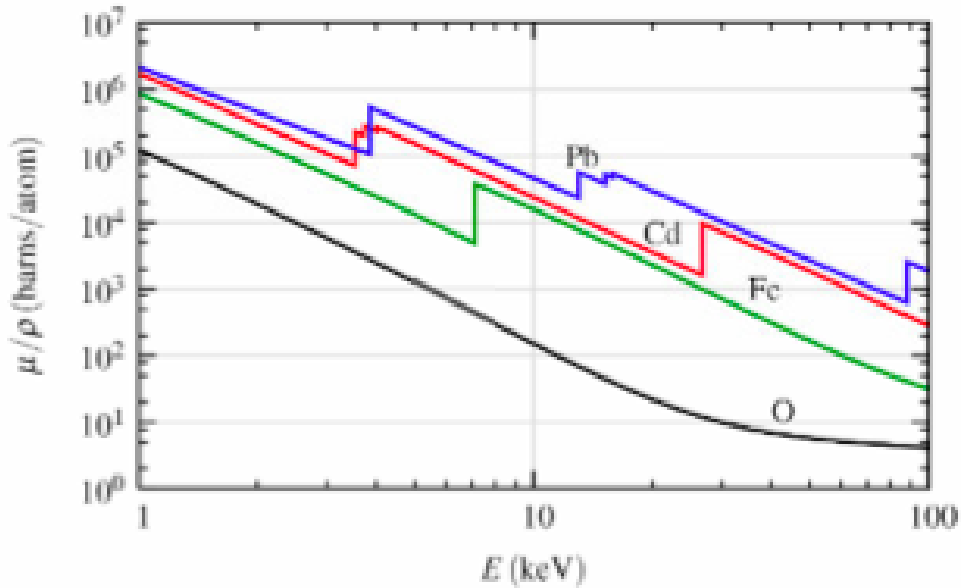


Figure 3.12: Mass/density coefficient as a function of photon energy for different elements [35].

This discontinuity is the result of a core electron absorbing energy that is equal to or greater than its binding energy, exciting it up to a vacant shell and leaving behind a core hole.

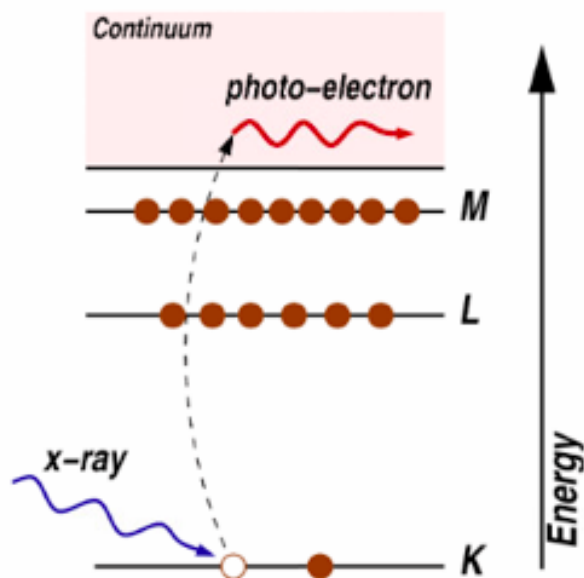


Figure 3.13: Diagram depicting x-ray absorption by a core electron [30].

When x-ray energies are scanned across one of these discontinuities, and plotted as a function of x-ray energy (i.e. $-\ln(I/I_0)$ vs E), a sharp rise, or edge, will be observed at the binding energy of that shell, known as the “white line”. This edge jump is named by the principle quantum number of the specific core electron being excited [30]:

Table 3.2: X-ray absorption edge and its corresponding electron orbital.

K-edge	1s			
L-edge	2s	2p		
M-edge	3s	3p	3d	
N-edge	3s	3p	3d	3f

XAS can be broken down into two different regions, X-ray Absorption Near Edge Spectroscopy (XANES), which is the part of the spectrum that ranges from about 50 eV below the edge to about 50 eV above the edge; and Extended X-ray Absorption Fine Structure (EXAFS), which is the region of the spectrum that ranges from 50 eV above the edge up to about 1000 eV above the edge as shown in the following figure:

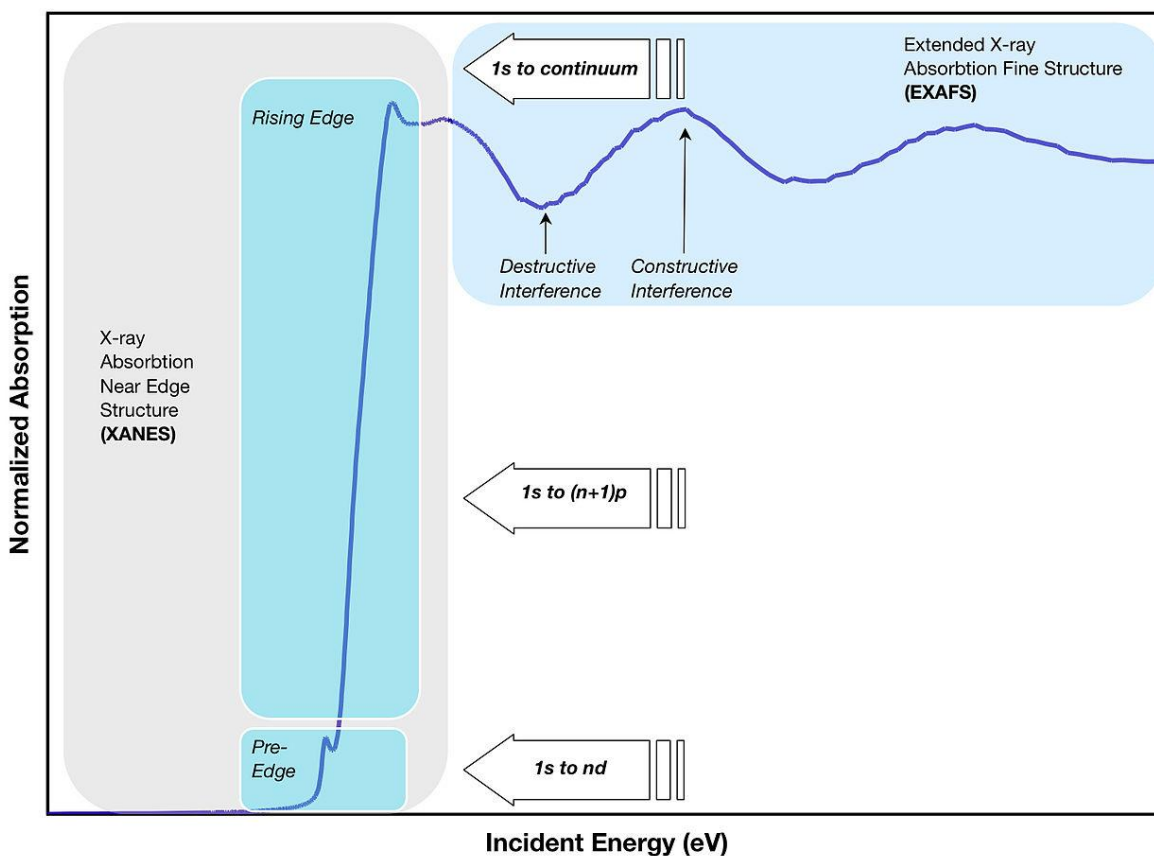


Figure 3.14: Typical XAFS spectrum broken down into its different regions [31].

XANES probes the unoccupied subshells of an atom based on exciting core electrons, typically the K or L electrons, into an unoccupied shell of higher energy based on allowed dipole transitions, or $\Delta l = \pm 1$, $\Delta j = \pm 1$, and $\Delta s = 0$, where l is azimuthal quantum number, and j is the

total angular momentum quantum number. As the spin does not change, the electron must be excited into a shell with a different azimuthal quantum number. These selection rules are shown in the following table [30]:

Table 3.3: Selection rules for core electron transitions.

Initial State	Final State
S	p
P	s, d
D	p, f
F	d, g

The following figure shows the energy of the different x-ray absorption edges as a function of absorption intensities, which can also be considered as transition probabilities.

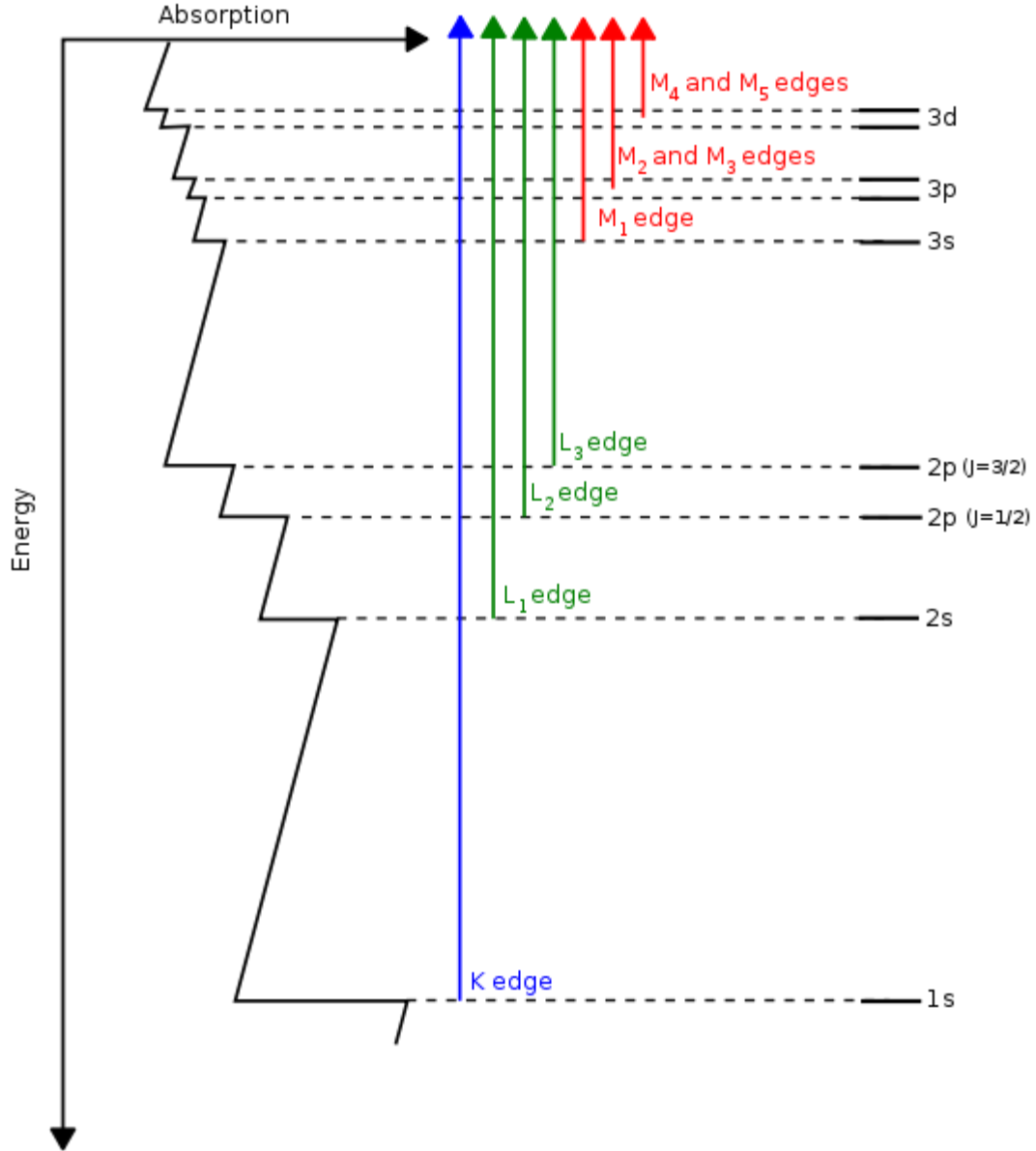


Figure 3.15: Visual representation of table 2, along with transition probabilities [34].

It should be stated that the absorption effect requires that the core electron be excited into an unoccupied state. So the 1s electrons must be excited into the lowest unoccupied p shell [30]. The experiments of this thesis are based around the 1s transition, or K-edge XAS.

XANES can yield large amounts of information pertaining to the oxidation state of valence electrons, as well as vacant shell and electron densities. The edge will shift upward in energy with higher oxidation states due to the fact that as more valence electrons contribute to bonding, their shielding effect on the nucleus becomes less pronounced, causing the bond length to decrease. The energy required to excite core electrons into the continuum will increase as $1/R^2$, causing the edge energy to increase. The intensity of specific XANES features can also yield information about the electron densities of given orbital.

Whereas XANES is sensitive to the electronic environment of the absorbing atom, such as oxidation state and electron densities, EXAFS is sensitive to local structure and molecular coordination. XANES is a phenomenon based on multi-pathway scattering of the excited core photoelectron wave off of its nearest neighbors, since the photoelectron wavelength is greater than the distances of the nearest neighbors. This allows for multiple scattering events before returning to the absorbing atom. Because of this, though structural information is present in the spectrum, it is very difficult to properly model. EXAFS on the other hand, is based off of single path scattering off of the nearest neighbors of the absorbing atom, since the wavelength approaches and becomes greater than that of the nearest neighbors [35]. This is demonstrated in the following figure.

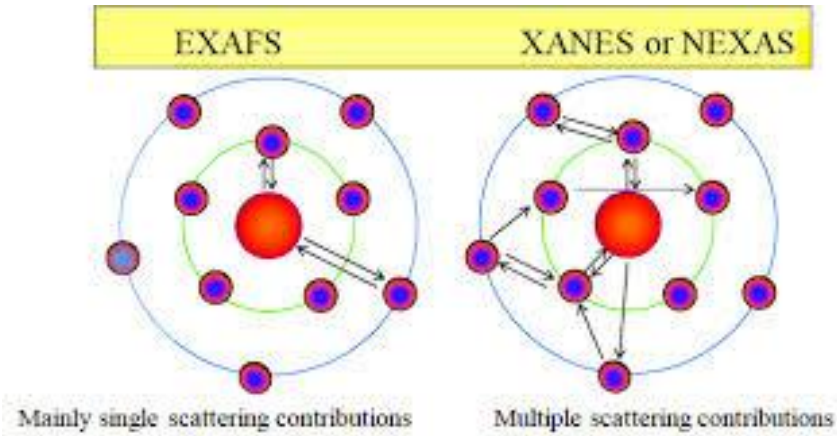


Figure 3.16: Diagram depicting the difference between the scattering that leads to the different types of the XAFS spectrum [35].

The EXAFS spectrum is the result of a core electron being excited into a vacant shell, causing it to be emitted as a photoelectron with energy of

$$E - E_0 = \frac{p_e^2}{2m_e} \quad \text{Equation 3.26}$$

Where E is the energy of the exciting x-ray, E_0 is the binding energy of the core electron, p_e is the momentum of the electron, and m_e is the electron rest mass. Due to the wave nature of the photoelectron, its wavelength can be expressed by the following:

$$\lambda_e = \frac{h}{p_e} = \frac{h}{\sqrt{2m_e(E-E_0)}} \quad \text{Equation 3.27}$$

This photoelectron back scatters off of a neighboring atom, and is reabsorbed by the absorbing atom. When this occurs, it perturbs the valence electrons, slightly changing the absorption coefficient. This slight perturbation changes the energy of the next photoelectron emitted. Due to the wave nature of the photoelectrons, the emitted photoelectrons will interfere with the scattered

photoelectrons; constructively if the waves are in phase, and destructively if they are out of phase, as illustrated in the following figure:

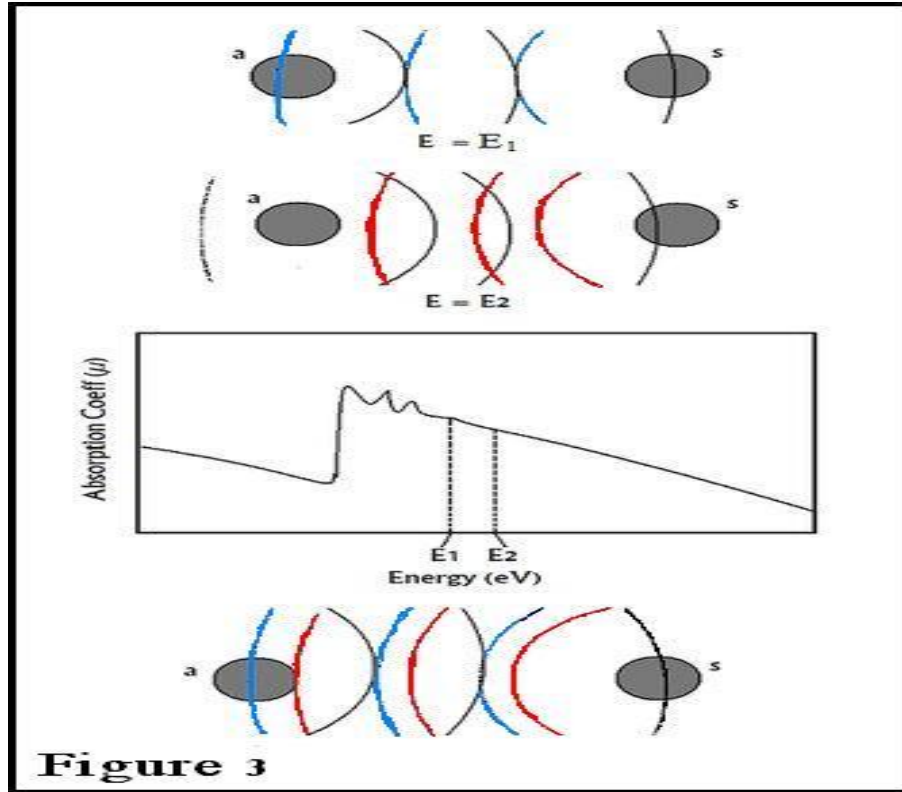


Figure 3.17: Diagram visualizing the phenomenon that leads to the EXAFS effect [35].

Due to the wave nature of the photoelectron, it is more useful to convert the energy spectrum into k space, where k has the units of \AA^{-1} , and can be expressed by the following:

$$k = \frac{\sqrt{2m_e(E-E_0)}}{\hbar} \quad \text{Equation 3.28}$$

The photoelectron wave must travel a distance of $2R_{as}$, or $2R_{as}/\lambda_e$ wavelengths, corresponding to a phase shift of:

$$\frac{4\pi R_{as}}{\lambda_e} = 2kR_{as} \quad \text{Equation 3.29}$$

Here, R_{as} is the distance between the absorbing atom and the scattering atom. This is the phase difference between the absorbing and scattering atoms, but the scatter event also creates a phase shift in the photoelectron wave that must be accounted for. This phase shift, $\delta(k)$, is based off of the structure factor of the atom. Correcting for this gives a total phase shift of the photoelectron wave as:

$$2kR_{as} + \delta(k) \quad \text{Equation 3.30}$$

The analysis of XANES is mostly qualitative in nature, though electron density of states can be calculated, whereas EXAFS can be physically modeled. The EXAFS region can be represented by the following function:

$$\chi(E) = \frac{\mu(E) - \mu_0(E)}{\Delta\mu(E)} \quad \text{Equation 3.31}$$

Here, $\mu(E)$ is the interference modified absorption coefficient at a specific energy, $\mu_0(E)$ is the background absorption coefficient of just the lone absorbing element, and $\Delta\mu(E)$ is the change in absorption across the edge and is used for normalization.

To derive $\chi(k)$, Fermi's golden rule must be used [30], but for the purpose of this thesis, I will skip the derivation. After applying the golden rule, and correcting for inelastic scattering, the EXAFS equation becomes:

$$\chi(k) = \sum_j \frac{N_j e^{-2R_j/\lambda(k)} e^{-k^2\sigma^2} f(k)}{kR_j^2} \sin [2kR_j + \delta_j(k)] \quad \text{Equation 3.32}$$

Where j represents the individual coordination shell of identical atoms at approximately the same distance from the absorbing atom, N is the coordination number, or the number of nearest neighbors, σ^2 is the mean-square displacement in the bond distance R . $\delta(k)$ has been explained earlier in this thesis, and $f(k)$ is the structure factor that determines the intensity of a scattered photoelectron wave and is based on atomic arrangements and electron densities of the neighboring atoms. A correction needs to be added in order to account for inelastic scattering off of the neighboring atoms.

As this is a summation over the different distances for each coordination shell, a Fourier transform must be performed in order to extract information about the distances to each of the nearest neighbors. There is no direct way to fit the data to known databases as in x-ray diffraction data, thus, in order to extract information about your system, different models must be created and compared to experimental data in order to extract information from the EXAFS equation. The structure factor $f(k)$ and phase shift factor $\delta(k)$ can be determined from x-ray crystallographic data, the coordination number N can also be extracted from crystallographic data, and the values R and σ can be determined by systematically generating different models using different values and comparing the results to experimental data.

Because of its ability to extract information about both oxidation and electron densities, as well as the ability to extract local structure information, XAS is a very powerful tool that can be used to extract extremely useful information in systems that are difficult to probe with other techniques.

Chapter 4

Experimental Section

4.1 High Pressure X-ray Absorption Spectroscopy Experiment

The first stage of my studies consisted of conducting a high pressure X-ray Absorption Spectroscopy (XAS) experiment. A panoramic-style diamond anvil cell with a beryllium gasket pre-indented to 50 μm , and laser drilled with a 120 μm hole. This hole was then loaded with a 1:1 ratio (by mass) mixture of potassium tetrafluoroborate (Sigma-Aldrich >99%) and cesium fluoride (Sigma-Aldrich 99%) under an argon atmosphere. It should be noted that cesium has an absorption length of 192 microns at its K-edge of 35985 eV. It was decided that ensuring a small enough hole size to allow for higher pressure to be achieved was crucial, and that a hole diameter of 120 μm would still allow for about 50% absorption across the K-edge, yielding a high enough signal to noise for analysis. Adding in KBF_4 decreased the effected cesium containing sample length, but initial testing still showed a 50% absorption across the edge. A small 20 μm , thermally relieved ruby sphere was placed in with the sample for pressure measurments. The cell was sealed and pressurized to 3 GPa in order to seal the mixture for irradiation, and allow for the formation of F_2 . The mixture was then irradiated at the 16 BM-B beamline at the Advanced Photon Source of Argonne National laboratory. “White” x-ray radiation in the 10 – 70 keV energy range was used to decompose the KBF_4 to produce molecular fluorine [15] to be used for reaction with the CsF to synthesize the novel CsF_n stoichiometric species. The sample was placed into the path of an unfocused 80 μm by 80 μm x-ray beam for approximately 8 hours.

The cell was then pressurized to 16 GPa and placed in the sector 16 BM-D beamline at the Advanced Photon Source of Argonne National Laboratory for x-ray absorption studies. The cell was placed perpendicularly to the beam path so absorption measurements could be made through the gasket along the length of the sample. A focused 8 μm by 8 μm monochromatic x-ray beam centered at the 35.985 KeV Cs k edge was used to probe the sample. The monochromator was scanned from 400 eV below the edge to 800 eV above the edge. The monochromator energy resolution was set to 4 eV up to 20 eV below the line, 1 eV from 20 eV below to 50 eV above the edge, 2 eV from 50 eV to 200 eV above the edge, and then 8 eV from 200 eV to 800 eV above the edge. Photon counting was done pre and post sample using ion chambers filled with a mixture of argon and xenon gas for initial and final x-ray intensity measurements. Measurements were made at 16, 53, and 69 GPa. Seven scans were performed at the three different pressures for signal averaging purposes.

The second study consisted of a high pressure XAS experiment of CsF (Sigma-Aldrich 99%) in order to have a comparison with the x-ray photochemistry experiment. A panoramic-style diamond anvil cell with a beryllium gasket pre-indented to 50 μm and laser drilled with a 120 μm hole was used. The hole was then loaded with cesium fluoride (Sigma-Aldrich 99%) under an argon atmosphere. A small 20 μm , thermally relieved ruby sphere was placed in with the sample for pressure measurements. The cell was pressurized to 2.7 GPa in order to ensure the sample was in its low pressure f.c.c. NaCl phase. The cell was placed perpendicularly to the beam path so absorption measurements through the gasket along the length of the sample could be made. A focused 8 μm by 8 μm monochromatic x-ray beam centered at the 35.985 keV Cs k edge was used to probe the sample. The monochromator was scanned from 400 eV below the edge to 800 eV above the edge. The monochromator energy resolution was set to 4 eV up to 20

eV below the edge, 1 eV from 20 eV below to 50 eV above the edge, 2 eV from 50 eV to 200 eV above the edge, and then 4 eV from 200 eV to 800 eV above the edge. Photon counting was performed pre- and post= sample using ion chambers filled with a mixture of argon and xenon gas for initial and final x-ray intensity measurements. Measurements were made at 2.7, 12.6, 25, 43, 55, and 68 GPa. Three scans were performed at the different pressures for signal averaging purposes.

The third absorption experiment consisted of a high pressure XAS experiment in order to repeat the first experiment, and attempt to obtain better data for fitting and modeling purposes. A Mao-Bell style diamond anvil cell with a beryllium gasket pre-indented to 50 μm laser drilled with a 120 μm hole was loaded with a 1:1 ratio by mass mixture of potassium tetrafluoroborate (Sigma-Aldrich >99%) and cesium fluoride (Sigma-Aldrich 99%) under an argon atmosphere. A small amount of gold powder (Sigma-Aldrich 99.999%) was placed with the sample for pressure measurements. The cell was sealed and pressurized to 3 GPa in order to seal the mixture for irradiation, but still keep the CsF in its B1 phase. A standard was also prepared at the same time. CsF was pulverized using a mortar and pestle into a fine powder and placed in Kapton® tape to protect it from contact with the atmosphere. The mixture was then irradiated at the sector 16 ID-B beamline at the Advanced Photon Source of Argonne National laboratory. Monochromatic x-ray radiation of wavelength 0.406626 Å (30.491 keV) was used to decompose the KBF_4 to produce molecular fluorine which was then used for reaction with the CsF to synthesize the novel CsF_n compounds. The sample was placed into the path of a focused 8 μm by 12 μm x-ray beam for approximately 12 hours.

The cell was then placed in the 16 BM-D beamline at the Advanced Photon Source of Argonne National Laboratory. The cell was placed perpendicularly to the beam path so absorption measurements through the gasket along the length of the sample could be made. A focused 6 μm by 10 μm monochromatic x-ray beam centered at the 35.985 keV Cs K-edge was used to probe the sample. The monochromator was scanned from 400 eV below the edge to 800 eV above the edge. The monochromator energy resolution was set to 4 eV from 400 eV to 20 eV below the edge, 1 eV from 20 eV below to 50 eV above the edge, 2 eV from 50 eV to 200 eV above the edge, and then 4 eV from 200 eV to 800 eV above the edge. Photon counting was accomplished pre- and post-sample using a mixture of argon and xenon gas filled ion chambers for initial and final x-ray intensity measurements. Measurements were made at 3, 16, 36, 46, 58, 64, 70 GPa, and then at 2.5 GPa post decompression from 70 GPa. Seven scans were performed at each of the different pressures for signal averaging purposes. Scans were also recorded of the standard pre- and post- experiment in order to test energy reproducibility of the monochromator, and to verify any shift in the spectrum edge.

4.2: Raman Spectroscopy Experiment

For the first Raman experiment, the cell from the third XANES experiment was used. Raman spectra were acquired using a Coherent® diode-pumped laser operating at 532 nm with a Triax 550® series spectrometer coupled to a Princeton Instruments® Peltier cooled charge coupled device (CCD) detector in the Raman facility at HP-CAT. The Raman spectrometer instrumental resolution was approximately 1 cm^{-1} . A 55:45 Transmission : Reflectance pellicle beam splitter was used to reflect the excitation source down along the collection axis. The light was focused down to an ~ 5 μm spot on the sample confined within the DAC containing ultra low fluorescence diamonds using a Mitutoyo 20x microscope objective with a working distance of

approximately 3 cm. Scattered light was then collected and collimated by the objective and sent back down the axis of excitation. A 92:8 pellicle beam splitter was used to reflect a small amount of light to a lens that focused the visible light onto a CCD camera based viewing system. The remaining scattered light was allowed to transmit through the two pellicles and was collected by a lens, which focused the scattered light onto a 150 μm vertical slit. The scattered light was then diffracted from an 1800 mm^{-1} diffraction grating blazed for optimum transmission in the visible range. The light was then collected by a focusing mirror, which focused the dispersed light onto a Peltier cooled CCD for imaging. The Raman spectrometer instrumental resolution was $\sim 1 \text{ cm}^{-1}$. The first Raman spectra was taken after the cell had been pressurized to 70 GPa and decompressed back down to 2.5 GPa. The sample was extremely fluorescent due to both x-ray irradiation damage, and strain to the molecular structure due to high pressure, causing delocalization of the electron structures within the bond. A single spectrum was acquired that was of acceptable quality, though spectra were acquired from multiple locations.

A second Raman experiment was performed at the Pravica group Raman facility at UNLV. The laser power source consisted of a Spectra Physics® Ar ion laser tuned to 514.5 nm laser line set at 100 mW (20 mW at the sample). A Jobin Yvon U1000® spectrometer utilizing the Czerny-Turner diffraction configuration, dispersed the scattered light which was then stored via an ISA Instruments Spectrum One® detector. The excitation configuration was a 180° backscattering configuration.

The collection configuration consisted of a laser bandpass filtration cube tuned to 514.5 nm that is used to filter out plasma lines emitted from the laser that are close to the laser line. A 55:45 Transmission:Reflectance pellicle beam splitter was used to reflect the excitation source further down the collection axis. The light was focused down to a $\sim 2 \mu\text{m}$ spot on the sample

confined within the DAC containing ultra low fluorescence diamonds using a Mitutoyo 10x microscope objective with a working distance of approximately 3.5 cm. Scattered light was then collected and collimated by this objective and reflected down the axis of excitation. A 92:8 pellicle beam splitter was used to reflect a small amount of light to a lens that focused the visible light onto a CCD camera based viewing system. The rest of the scattered light was allowed to transmit through the two pellicles and was collected by a lens, which focused the scattered light onto a 150 μm vertical slit. The scattered light was then diffracted from a 1800 mm^{-1} diffraction grating blazed for optimum transmission in the visible range. The diffracted light was then collected by a collimating mirror and reflected onto a second grating of the exact same configuration. This doubly diffracted light was then collected by a focusing mirror, which focused the dispersed light onto a liquid nitrogen cooled CCD for imaging. The Raman spectrometer instrumental resolution was $\sim 1 \text{ cm}^{-1}$. The Rayleigh scattered light was filtered using a Kaiser optics® 514.5 nm holographic notch filter with a bandwidth of $\sim 300 \text{ cm}^{-1}$. Acquisitions typically required 60 sec to complete. A Mao-Bell style diamond anvil cell was used along with a 300 μm thick stainless steel gasket was used to pressurize and confine the sample. The diamonds used each had a culet diameter of $\sim 300 \mu\text{m}$ and were ultra low fluorescence type Ia quality. The sample-confining gasket was preindented to $\sim 50 \mu\text{m}$ thickness and a sample hole of diameter 100 μm was drilled via electric discharge machining. CsF (Sigma-Aldrich 99%) and a 10 μm ruby sphere used for pressure calibration were loaded into the sample chamber under an argon atmosphere and pressurized to 2.5 GPa in order to match the experimental parameters in the previous experiment. Raman spectra were then taken in order to get a reference of CsF. Once spectra were acquired, the cell was disassembled, cleaned, and then reloaded with KBF_4 in order to obtain similar reference spectra.

4.3: High Pressure X-ray Diffraction Experiment

A high pressure x-ray diffraction experiment was performed on CsF (Sigma-Aldrich 99%) in order to ascertain its high pressure behavior at the pressures that we were attempting in the chemistry experiment. A Mao-Bell style diamond anvil cell mounted with double beveled diamonds each with 150 μm culets was used. A rhenium gasket pre-indented to 15 μm was laser drilled with a 70 μm hole was loaded with cesium fluoride (Sigma-Aldrich 99%) under an argon atmosphere. A small amount of gold powder (Sigma-Aldrich 99.999%) was placed in with the sample for pressure measurements. No pressure transmitting medium was used in order to attempt to best match the non-hydrostatic conditions in the chemistry experiment. The cell was pressurized to 1.9 GPa in order to ensure that the sample was in its low pressure f.c.c. NaCl phase. Diffraction patterns were acquired at the advanced photon source sector 16 ID-B beamline using a high speed Pilatus® silicon semi-conductor based detector. Monochromatic x-rays of wavelength 0.406626 Å were used, and diffraction patterns were acquired for 60 seconds at each pressure. Multiple pressure points were taken up to the maximum pressure of 120 GPa. A pattern of the ambient standard was also taken in order to determine an accurate 0 GPa volume.

X-ray diffraction was also conducted alongside the XAS measurements at the Advanced Photon Source sector 16 BM-D beam line. After each absorption measurement, the diamond anvil cell was rotated by 90° and the argon/xenon ion chambers were removed in order to allow the x-rays to transmit through the diamonds along the axis of least strain in the sample. The monochromator was then tuned to a wavelength of 0.4264 Å, and diffraction patterns were taken

using a Mar345® image plate. The Mar345® image plate functions via a photo-sensitive phosphor that is capable of storing x-rays by its ability to have electrons pumped from the valence band into the conduction band where they can remain for hours to days. Red laser light stimulates the electrons back from into the valence band causing a blue photon to be emitted. This blue photon is read by a photomultiplier, giving a count proportional to the number of x-rays absorbed [36]. Each pattern was recorded for 120 seconds, after which the experimental configuration was reset for the next XAS measurement.

Chapter 5

Results and Discussion

5.1 Initial High Pressure X-ray Absorption Spectroscopy Experiment on Irradiated Mixture of Cesium Fluoride and Potassium Tetrafluoroborate

Once we successfully released molecular fluorine via the x-ray decomposition of KBF_4 (as shown in Figure 2.1), we utilized this technique to provide excess fluorine to react with CsF in order to potentially form novel CsF_n ($n > 1$) compounds at high pressure. My first attempt to synthesize a novel CsF_n compound showed promising results.

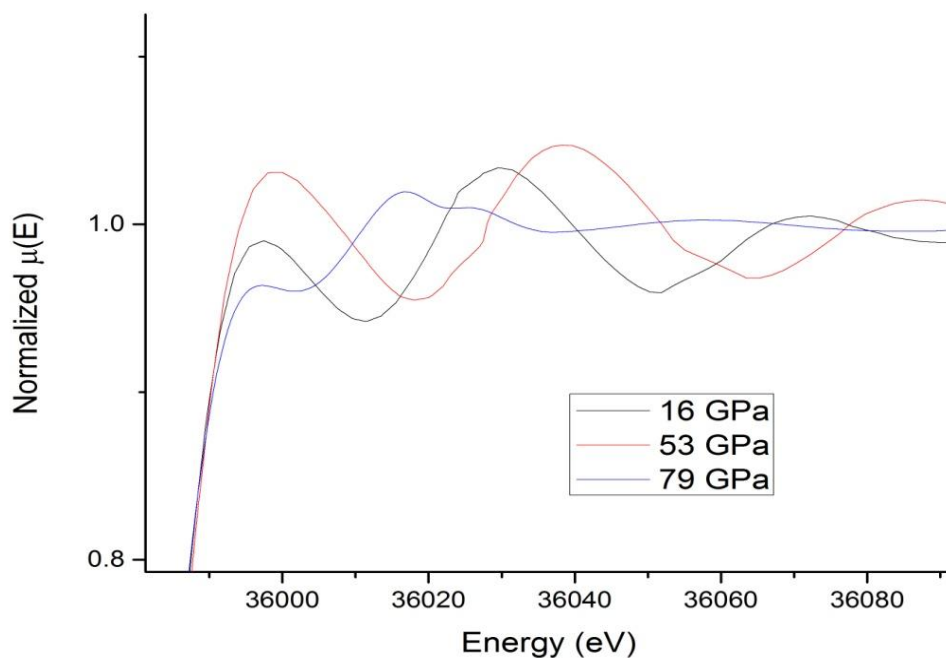


Figure 5.1: XANES spectra of mixture of CsF and KBF_4 from first experiment showing clear changes to the XANES spectrum at 70 GPa.

A systematic increase in the absorption coefficient from 16 to 53 GPa demonstrates a progressive increase in vacancies within the 5p orbital. This has been shown to occur in pure cesium under pressures above 3 GPa [19] and was discussed earlier in this thesis. At 70 GPa, which was post reaction, it can be seen that the white edge intensity drops quite dramatically, and the XANES feature shifts upward by approximately 20 eV. This observation, coupled with the drop in the first two low k EXAFS features of about 15 eV, showed strong evidence of novel chemistry occurring. This dramatic change can also be observed in Figure 5.2. In the transformation into k space, there is a shift up in wavenumbers between 16 and 53 GPa, which correlates to a shift down in the R space of the coordination shells; following a dramatic shift downward in wavenumbers at 70 GPa, attributing to a shift upward in R space of the coordination shells.

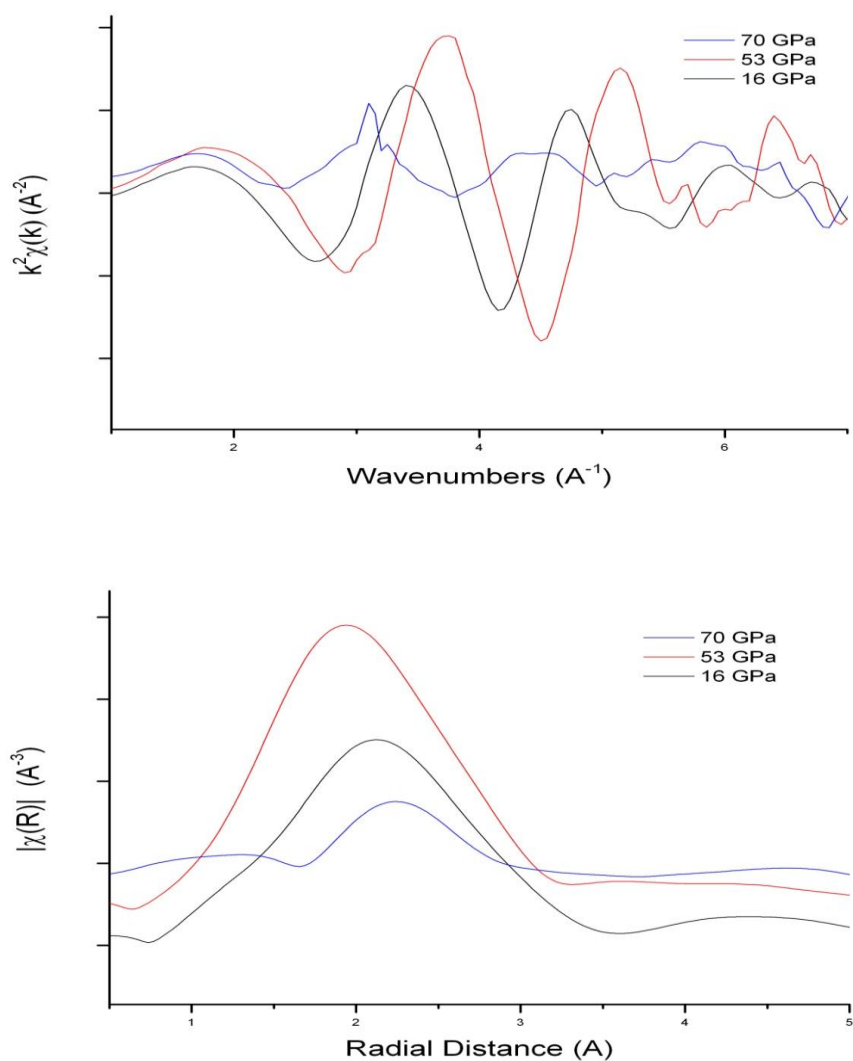


Figure 5.2: k-space transformation of low k EXAFS of data in figure 23 weighted by k^2 (top) and the magnitude of its Fourier transform into radial space (bottom).

Evidence of this possible chemical reaction can also be observed visually in Figure 5.3. Visible changes also occurred within the sample chamber of the x-ray photochemistry experiment that occurred after pressurizing to 70 GPa. The sample went from being a white semi-translucent color, to dark brown, providing further evidence for a chemical change in the sample

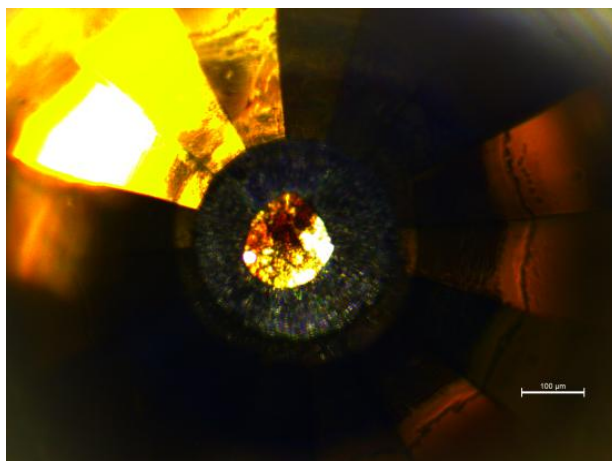


Figure 5.3: Image of irradiated mixture of CsF and KBF_4 pressurized to 70 GPa.

5.2: High Pressure X-ray Absorption Experiment of Pure Cesium Fluoride

In order to verify that the changes observed in the XAS spectrum of the irradiated mixture of CsF and KBF_4 were unique to the mixture and not a result of the CsF by itself, a baseline high pressure XAS experiment of pure CsF was performed up to 68 GPa. A systematic increase in both the absorption edge intensity that was seen in section 5.1, as well as a systematic increase in the low k EXAFS features, attributed to a systematic decrease in the intermolecular distances can be seen in figure 5.3. Though subtle, the phase transition from the B1 NaCl phase of CsF to the B2 CsCl phase occurs between 2.7 and 12.6 GPa.

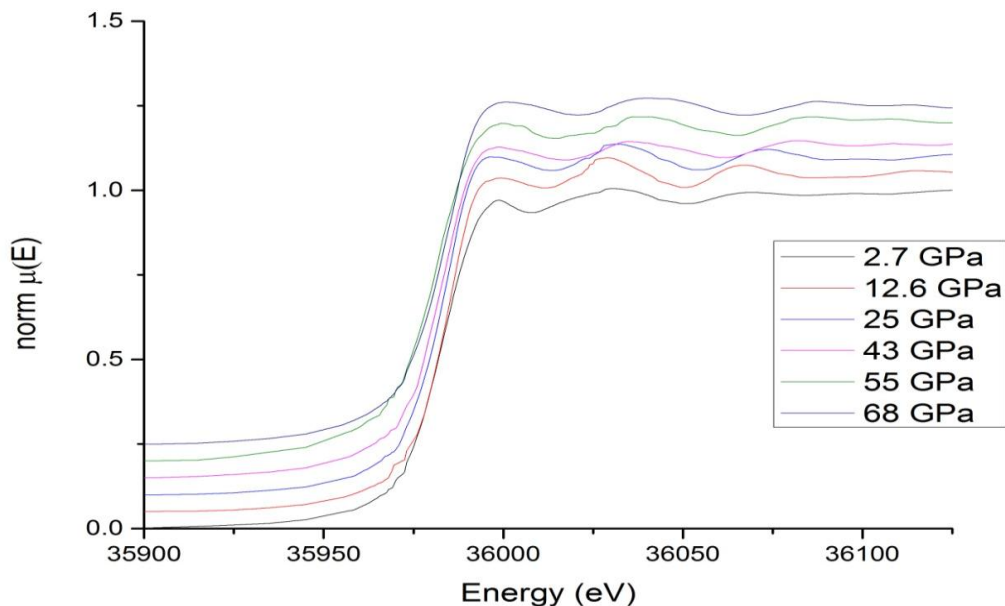


Figure 5.4: Low k XAS spectrum of pure CsF up to 68 GPa.

Modeling was performed courtesy of Dr. Ning Chen from the Canadian Light Source on the XANES data and low k EXAFS data in order to extract interatomic distances and unit cell parameters. Crystallographic data was used from the Inorganic Crystal Structure Database (ICSD) to extract structure factor information for modelling purposes. Figure 5.5 shows the best fit models to experimental data. *Ab initio* based calculations using the FDMNES® calculation package was used for modelling the XANES data. Figure 5.6 shows the best fit models to the low k EXAFS experimental data modeled using the FEFF® calculation package.

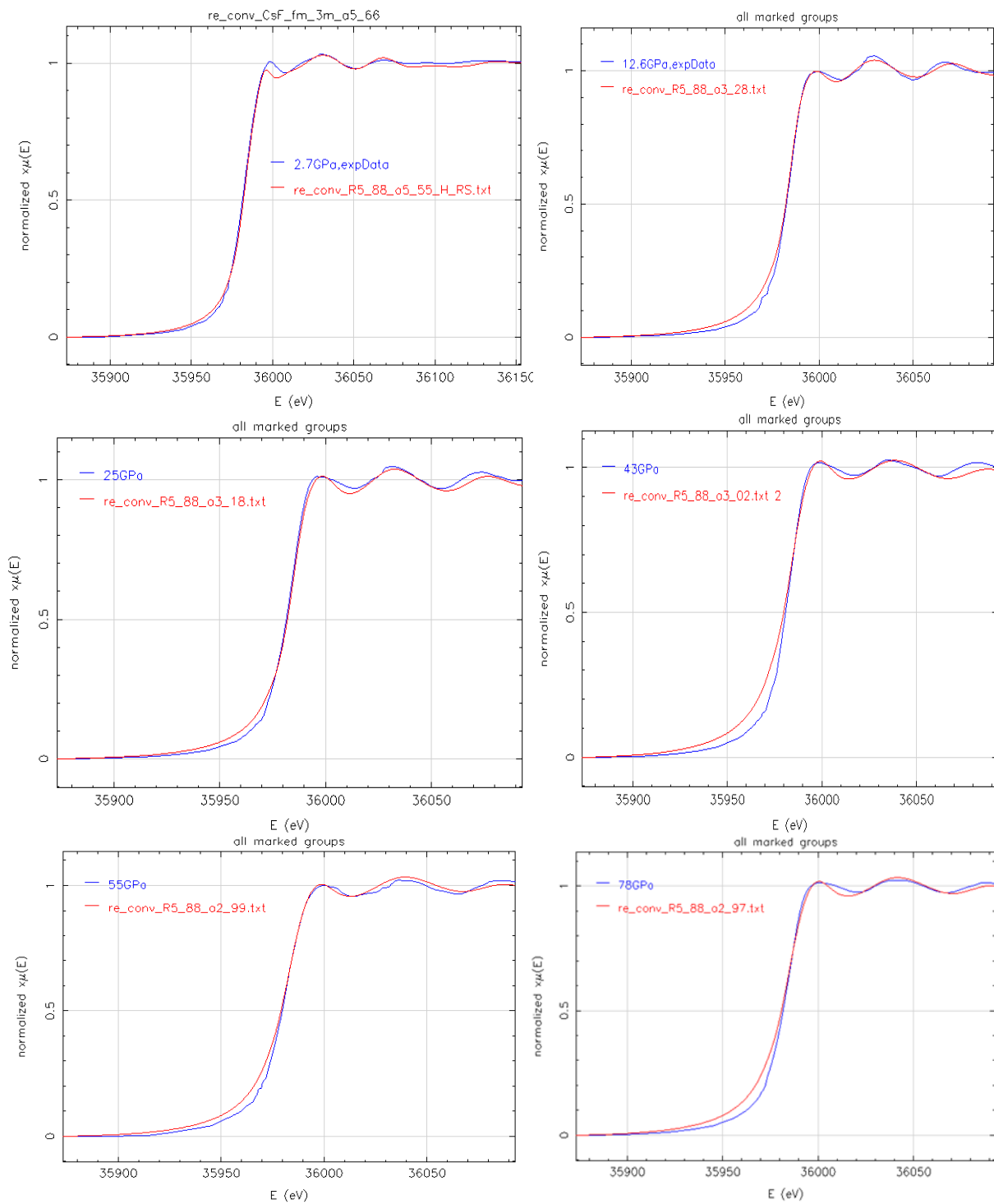


Figure 5.5: DFT based FDMNES® models that best fit to experimental XANES data courtesy of Dr. Ning Chen from the Canadian Light Source.

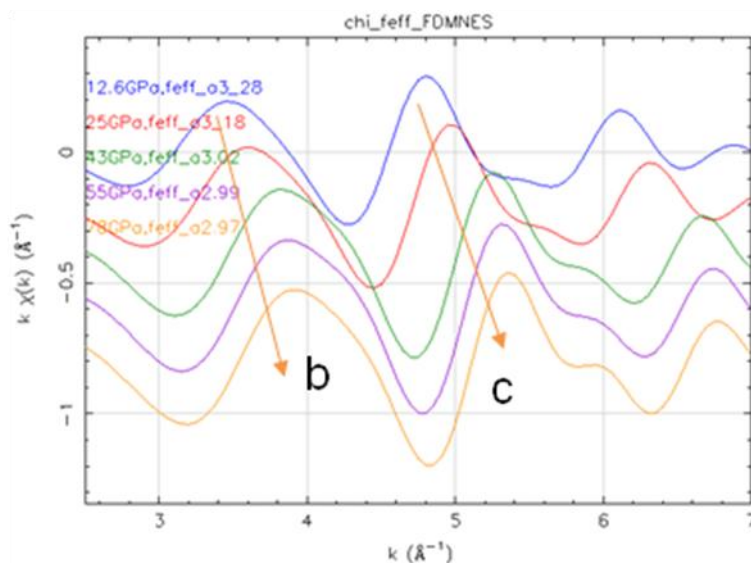


Figure 5.6: DFT based FEFF® models that best fit to experimental low k EXAFS data courtesy of Dr. Ning Chen from the Canadian Light Source.

From the best fit models, the EXAFS equation could be solved, extrapolating out the unit cell parameter ‘a’ for the B2 CsCl phase of CsF, as well as the interatomic distances for the first and second coordination shells around the absorbing cesium atoms. This information is displayed in Figure 5.7 and tabulated against the values given in the ICSD in Table 5.1.

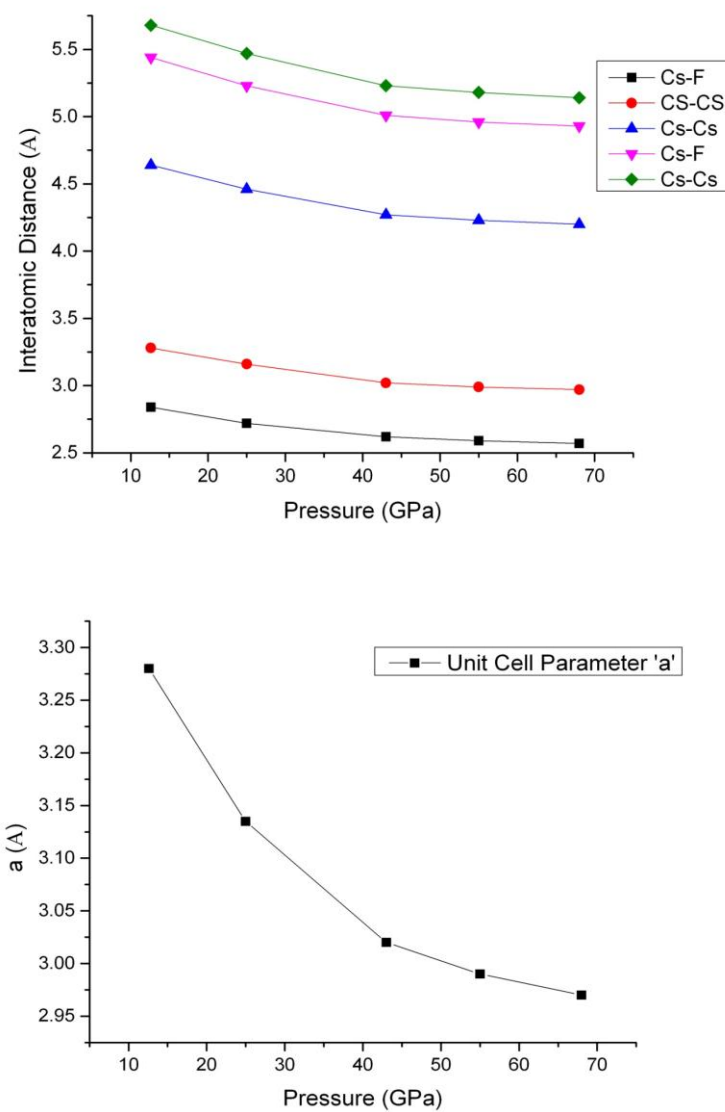


Figure 5.7: Calculated interatomic distances between the absorbing cesium atom and its nearest neighbor, and its nearest nearest neighbor (top) and the calculated unit cell parameter 'a' (bottom) for the CsF B2 phase as determined from the models in Figure 27.

Table 5.1: Summary the XANES modeling result for low and high pressure CsF phases.

Space group	Pressure (GPa)	a	Cs-F	Cs-Cs	Cs-Cs	Cs-F	Cs-Cs
fm-3m	44288-ICSD	6.12	3.06	4.32	n/a	5.30	6.12
	2.7GPa	5.66	2.83	4.00	n/a	4.90	5.66
pm-3m	61563-ICSD	3.39	2.94	3.39	4.79	5.62	5.87
	12.6GPa	3.28	2.84	3.28	4.64	5.44	5.68
	25.0GPa	3.18	2.75	3.18	4.50	5.27	5.51
	43.0GPa	3.02	2.62	3.02	4.27	5.01	5.23
	55.0GPa	2.99	2.59	2.99	4.23	4.96	5.18
	68.0GPa	2.97	2.57	2.97	4.20	4.93	5.14

In Figure 5.7 and Table 5.1, it is evident that pure CsF does not undergo any type of phase transition, electronic or structural, beyond its initial transition from B1 to B2 at 4.7 GPa, lending further evidence to the possibility of novel chemistry in the experiment discussed in section 5.1.

5.3 Second High Pressure X-ray Absorption Experiment on Irradiated Mixture of Cesium Fluoride and Potassium Tetrafluoroborate

A second attempt to synthesize novel CsF_n compounds was performed to both verify that the chemical reaction occurred in the same pressure range as the first experiment, as well as to attain more pressure points for a better understanding of the reaction.

Figure 5.8 shows the dramatic change in the XAS profile between 58 and 64 GPa. When comparing the XAS spectrum of the B1 $\text{fm}3\text{m}$ phase of pure CsF and the XAS spectrum of the sample post reaction which suggests that the sample underwent a coordination change into a structure similar to that of the B1 phase of CsF. The primary differences observed are a slight downshift in energy of the features labeled B and C in Figure 5.8, as well as a slight difference in the XANES feature labeled A.

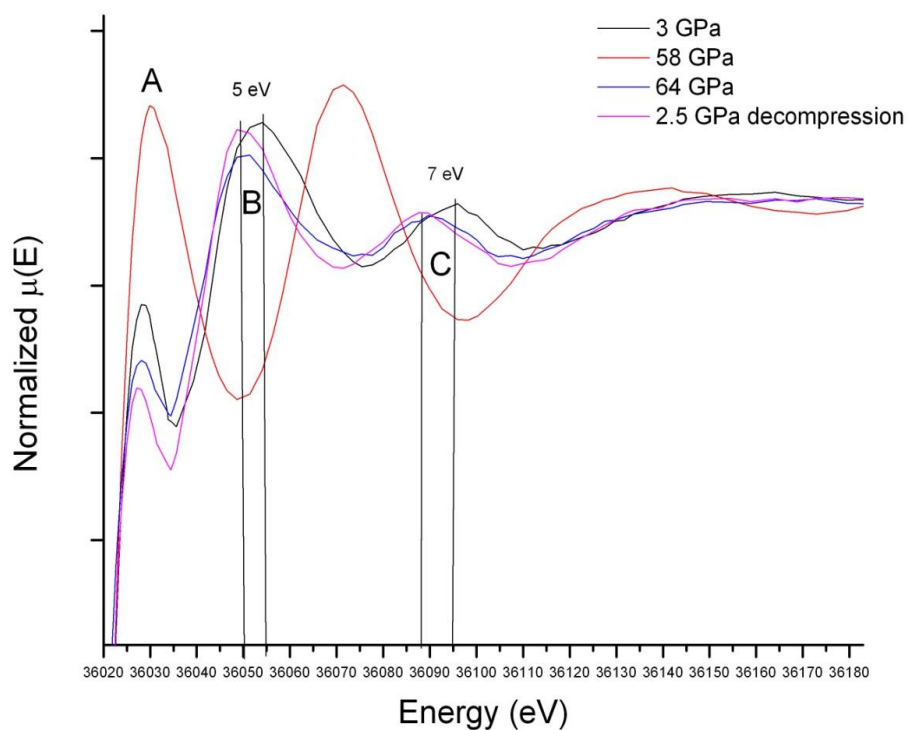


Figure 5.8: Low k XAS spectrum of a mixture of CsF and KBF₄ irradiated at 3 GPa, pressurized to 64 GPa and decompressed to 2.5 GPa.

The similarities between the data of the low pressure phase of CsF and the data above 58 GPa can be seen more vividly in the k space and R space transformations in Figure 5.9. The similarities between the standing wave behavior in the 3 GPa data of the pure CsF pre-reaction and the 64 GPa post reaction suggests that the compound formed at 64 GPa has a similar local coordination to that of the B1 phase of pure CsF with slightly larger distances between nearest neighbors, seen by the downshift in wavenumbers of the standing waves (5.9 top) and the slight increase in radial distances of the coordination shells (5.9 bottom). In order to verify the validity of the transformation from k space into R space, a reverse Fourier transform was performed on the radial data and plotted against the k space data. Figure 5.10 shows that each data point back transforms accurately, demonstrating the validity of the data in figure 5.9. It also appears that this reaction is irreversible based on the nearly identical spectra taken at 64 GPa and 2.5 GPa (post decompression).

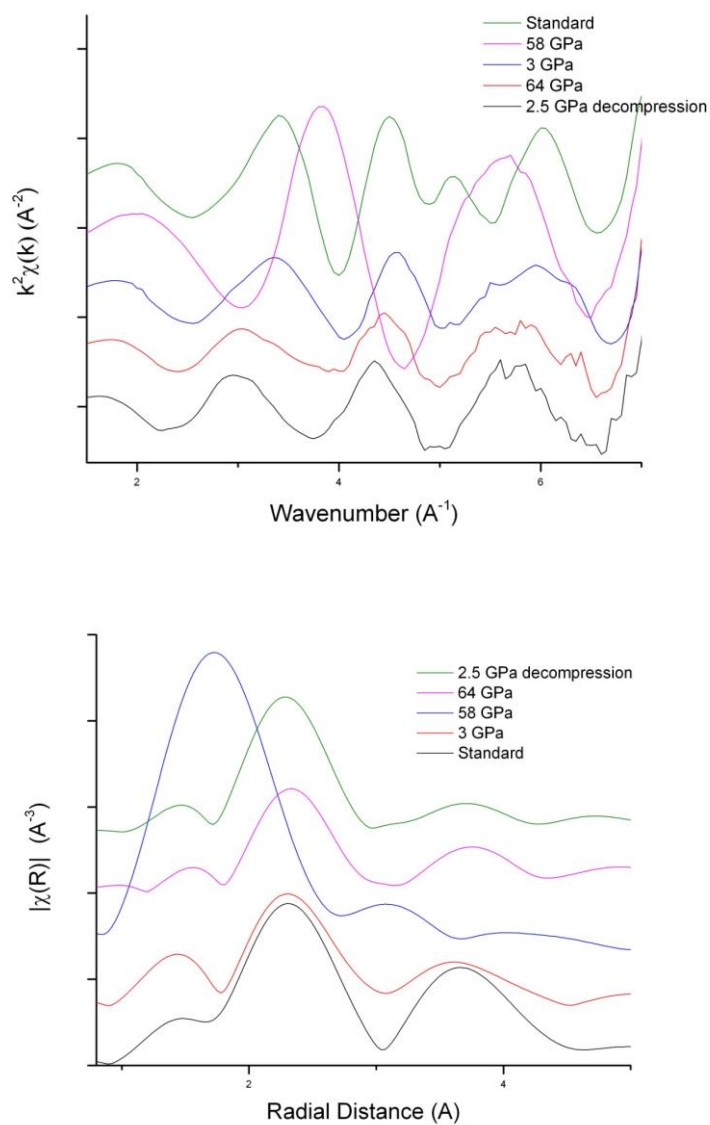


Figure 5.9: k-space conversion of data in figure 5.8 weighted by k^2 (top) and the magnitude of its Fourier transform into radial space (bottom).

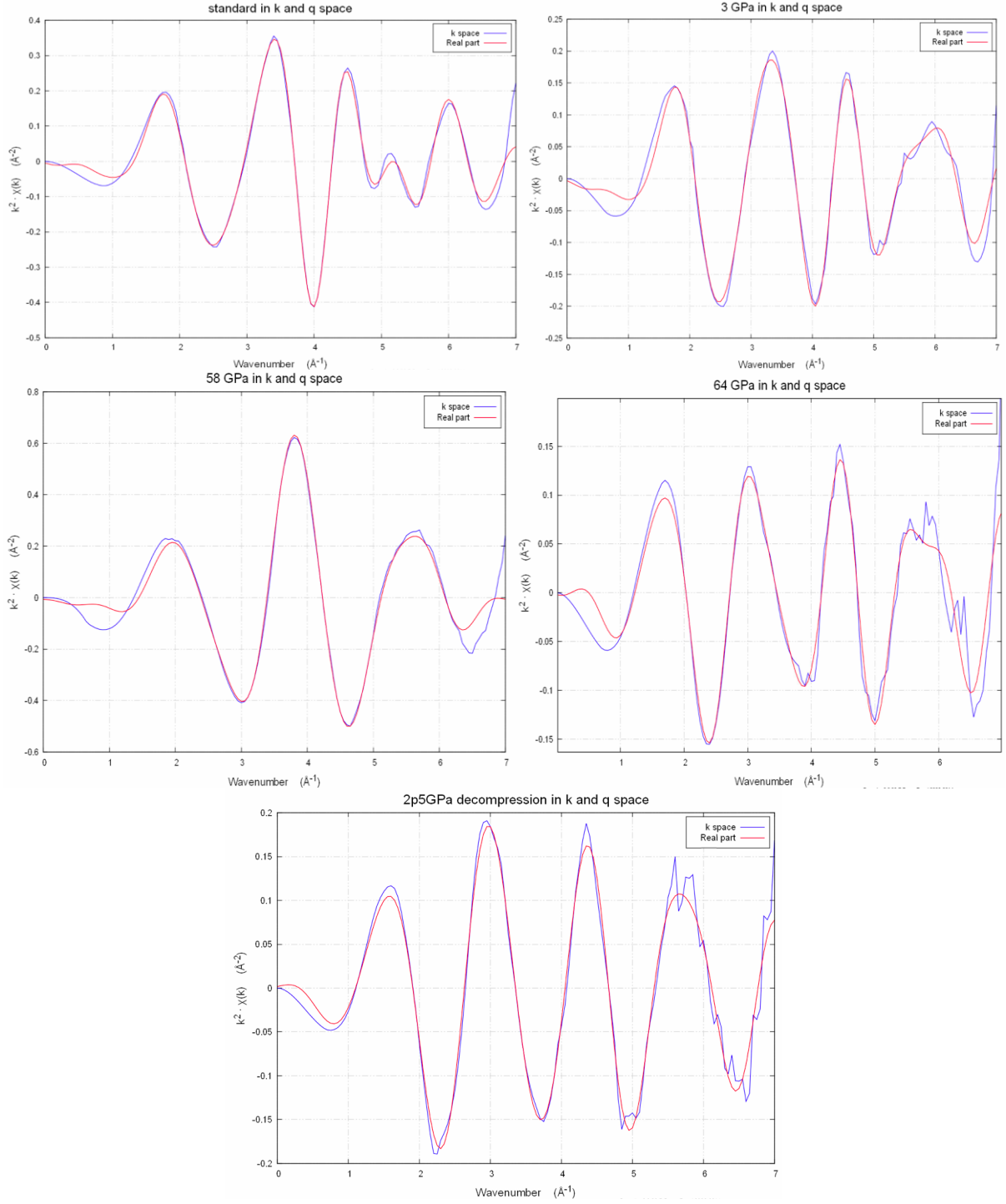


Figure 5.10: Reverse Fourier transforms of the R-space data shown in Figure 5.9 (bottom) plotted against the k-space transforms in Figure 5.9 (top).

As briefly discussed in section 5.1, pure cesium metal exhibits systematic spd hybridization under pressure via broadening of the 5p and 6s orbitals. This broadening leads to an overlapping of the 5p and 6s orbitals wavefunctions and a promotion of electron densities into the vacant 5d orbital. This hybridization effectively allows the 5p electrons to be utilized in bonding, leading to the formation of the CsF_n compounds. Figure 5.11 displays the systematic increase of vacancies in the 5p orbital of cesium, as well as a systematic broadening of the energy of the 5p orbital. There is an abrupt drop in the XANES edge intensity across the reaction at 64 GPa which suggest a sudden rise in electron density within the p orbital. This phenomenon can possibly be explained by the filling of the shell via the bonding with additional fluorine.

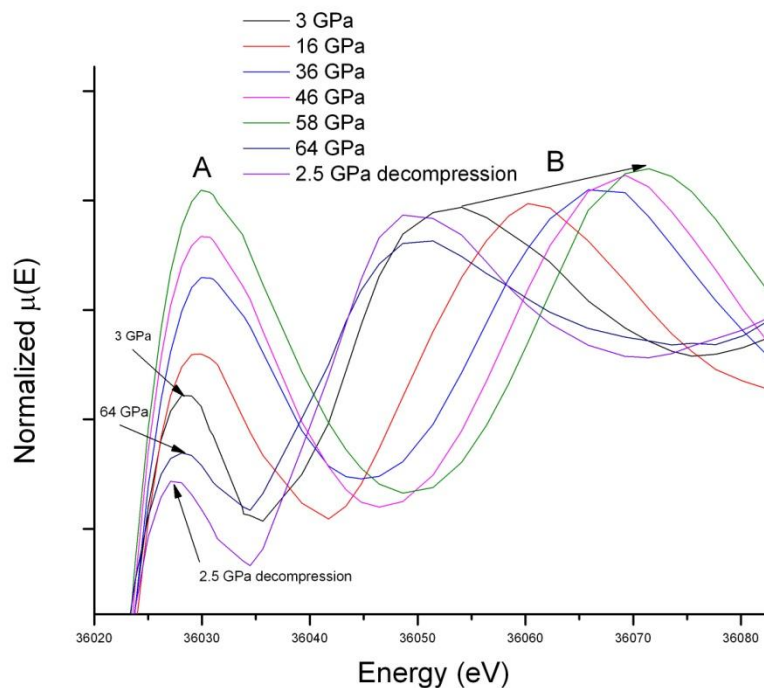


Figure 5.11: XANES spectrum of each pressure point in the second mixture experiment showing continuous increase in the XANES and low k EXAFS profile up until the onset of the reaction at 64 GPa.

In order to give further credence to novel chemistry occurring above 58 GPa, a model was created using crystallographic data obtained via x-ray diffraction of CsF to show that the XAS data in the mixture was still that of pure CsF at 58 GPa; this is shown in Figure 5.12. A model was also created of pure CsF at 67 GPa and compared to the experimental data of the mixture at 64 GPa, showing that our sample was no longer pure CsF; this is shown in Figure 5.13.

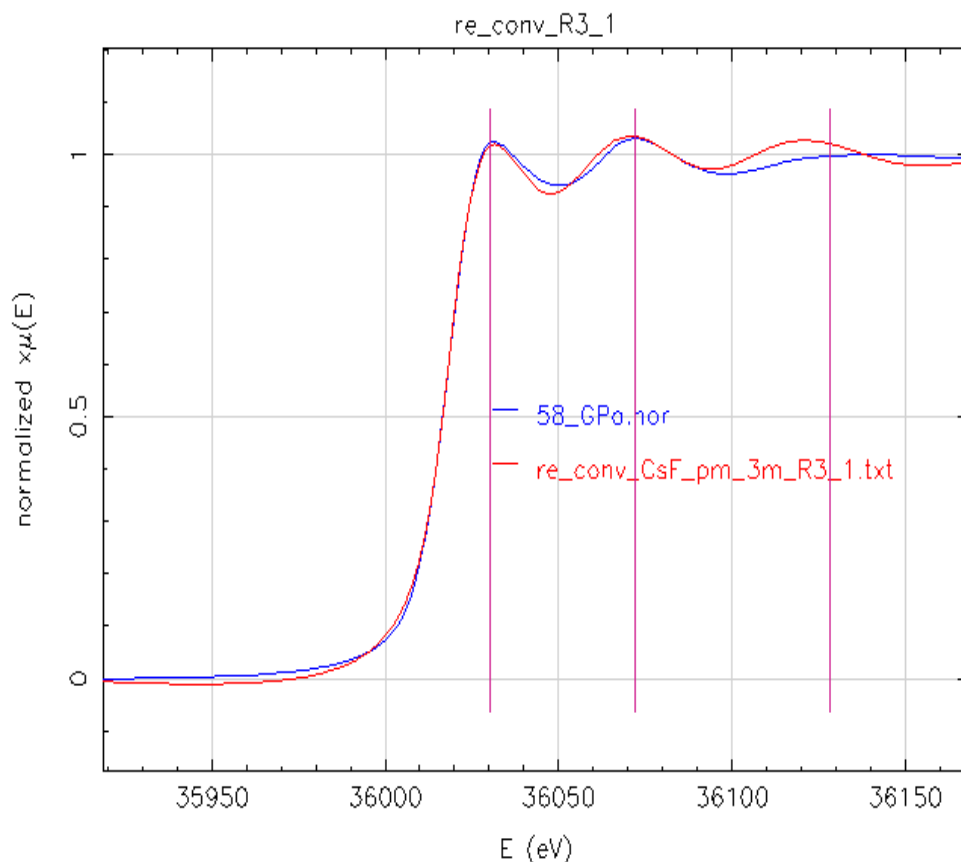


Figure 5.12: XAS experimental data of mixture plotted against the modeled XAS data using structural values determined in x-ray diffraction experiment showing that, at 58 GPa, the absorbing was still CsF and not a new compound.

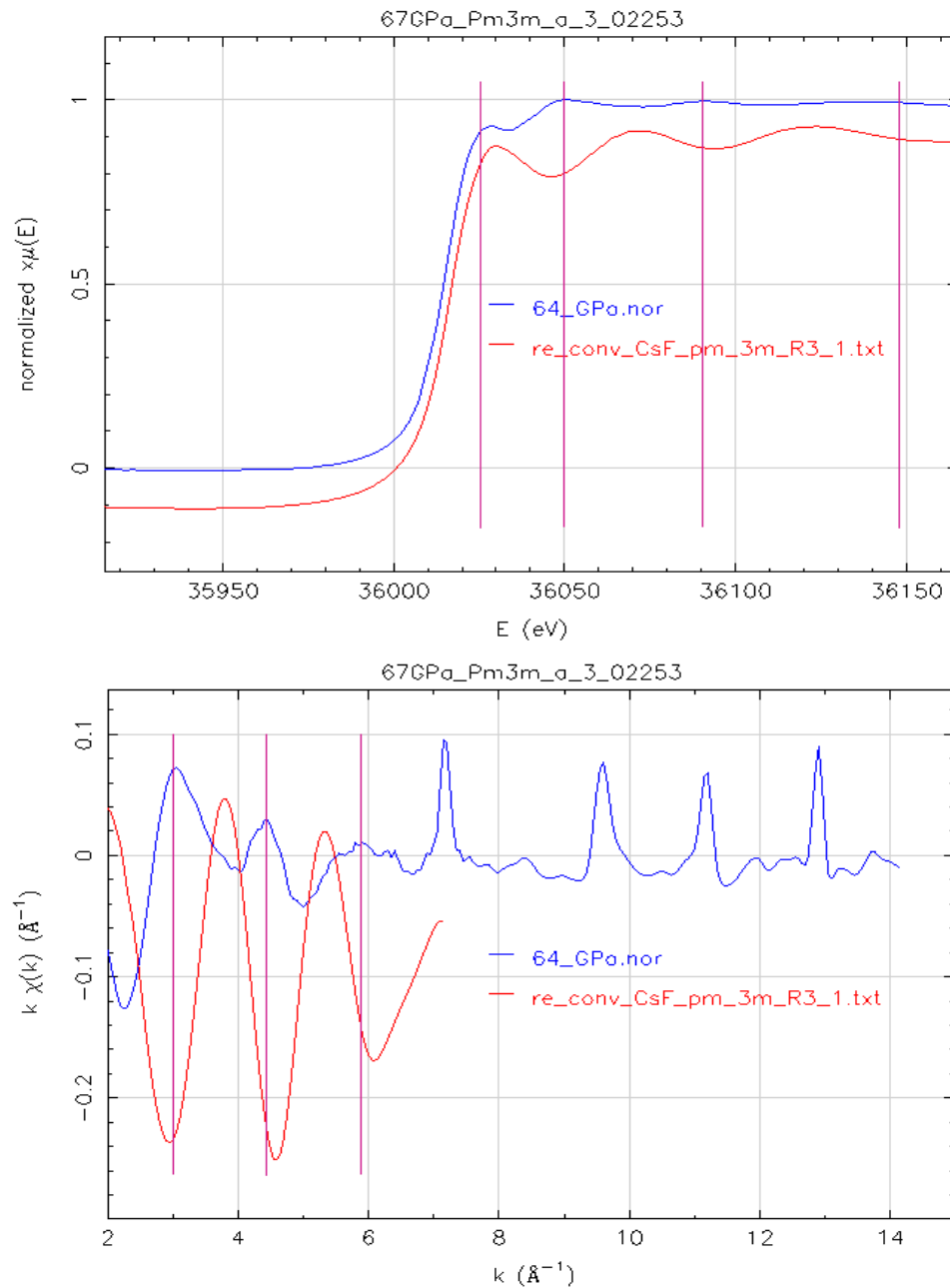


Figure 5.13: XAS (top) and low k EXAFS (bottom) Experimental data of the mixture of CsF and KBF_4 at 64 GPa plotted against a model of pure CsF based on diffraction data at 64 GPa.

Based on the similarities between the XAS spectra at 3 GPa and 64 GPa, we hypothesized that CsF_2 may have been synthesized in a CaF_2 structure. CaF_2 is an $\text{fm}3\text{m}$ structure [37], similar to that of the B1 phase of CsF, this similarity is presented in Figure 5.15.

Figure 5.14 shows models of CsF_2 created based off of the CaF_2 unit cell. Though the XAS data fits nicely to the experimental data at 64 GPa, models show that the best fit is with a unit cell parameter 'a' of approximately 7 Å, which is approximately 40 % larger than the 5.4 Å that was predicted by DFT calculations. This discrepancy can be explained by the fact that the reaction was incomplete, as shown via x-ray diffraction data in section 5.4. It is possible that, though the local coordination formed in the CaF_2 structure, the lattice was highly strained due to the conditions it was synthesized. Despite this discrepancy, the similarities in k and R space transforms of the experimental data still suggest a highly cubic structure. This along with the XANES behavior across the reaction gives good evidence for the formation of CsF_2 .

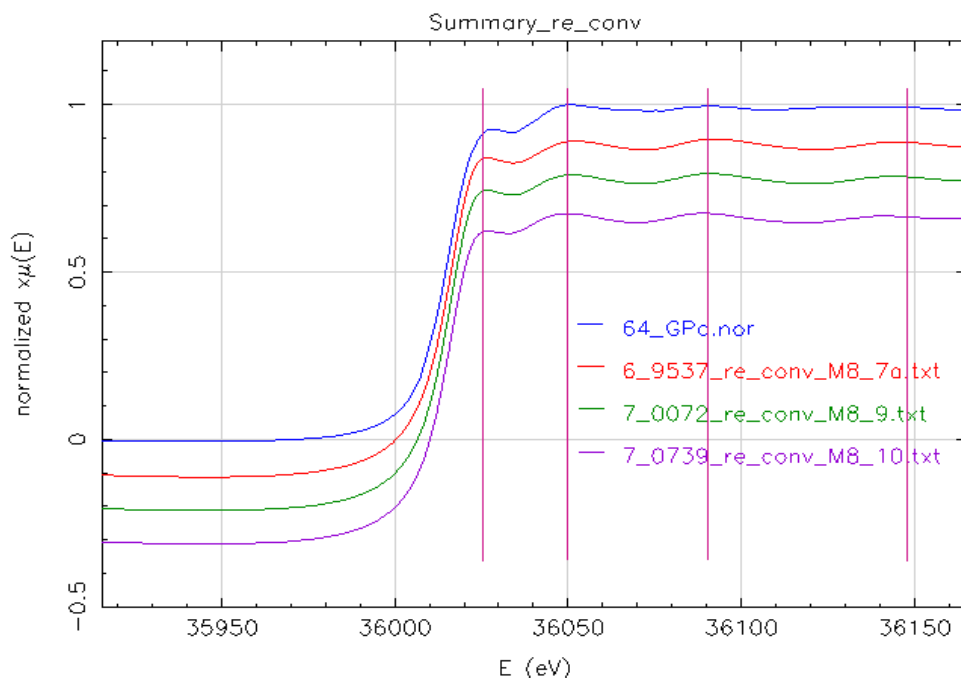


Figure 5.14: Experimental XAFS data of the mixture of CsF and KBF_4 modeled against the theoretical CsF_2 compound in the CaF_2 structure, showing the best fit data to be of a unit cell parameter 'a' of approximately 7 Å.

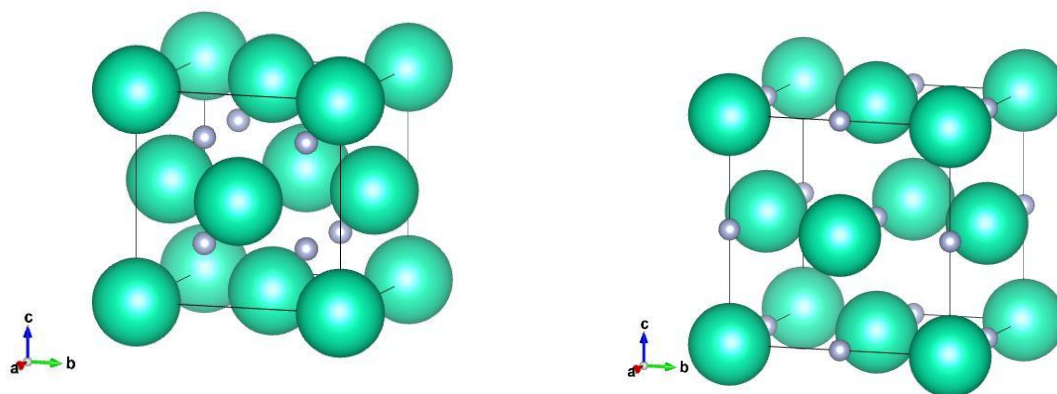


Figure 5.15: Graphical representations of the CsF_2 unit cell (left) and the B1 phase of the CsF unit cell, created by VESTA.

5.4: X-ray Diffraction study of Mixture of Cesium Fluoride and Potassium

Tetrafluoroborate at 64 GPa

As evident in Figures 5.15 and 5.16, the diffraction patterns of the mixture, post reaction, are extremely convoluted and difficult to interpret. The peaks can be explained somewhat by mixing the theoretical diffraction patterns for CsF_2 , CsF , KBF_4 , and gold. However, there are some areas, primarily in the low and high 2θ that do not match up very well. This may be due to the extremely non hydrostatic conditions the cell was under, along with the incomplete nature of the reaction leading to the formation of CsF_2 . It should be noted that, though gold can react with fluorine to form gold pentafluoride (AuF_5), this reaction only occurs under high temperature conditions, and the diffraction pattern shows that this reaction did not occur via the pristine gold diffraction peaks.

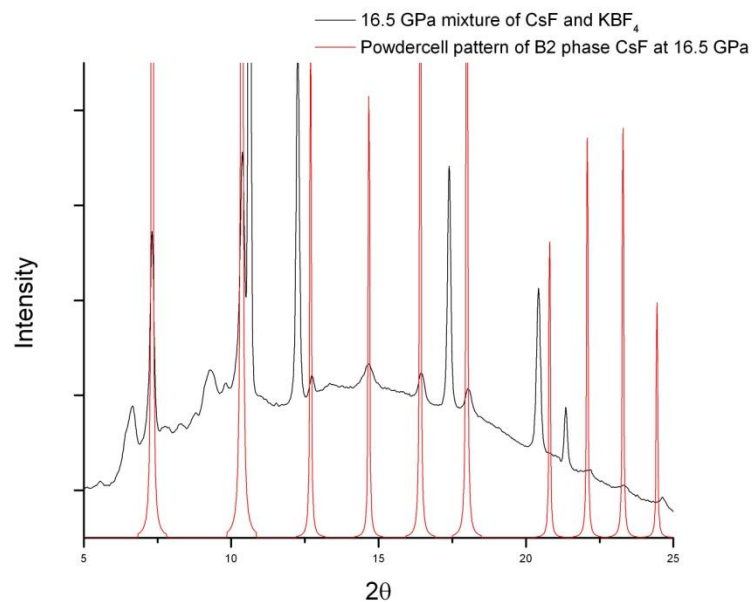


Figure 5.16: X-ray diffraction pattern of mixture of CsF and KBF₄ at 16.5 GPa showing presence of pure CsF in B2 CsCl phase.

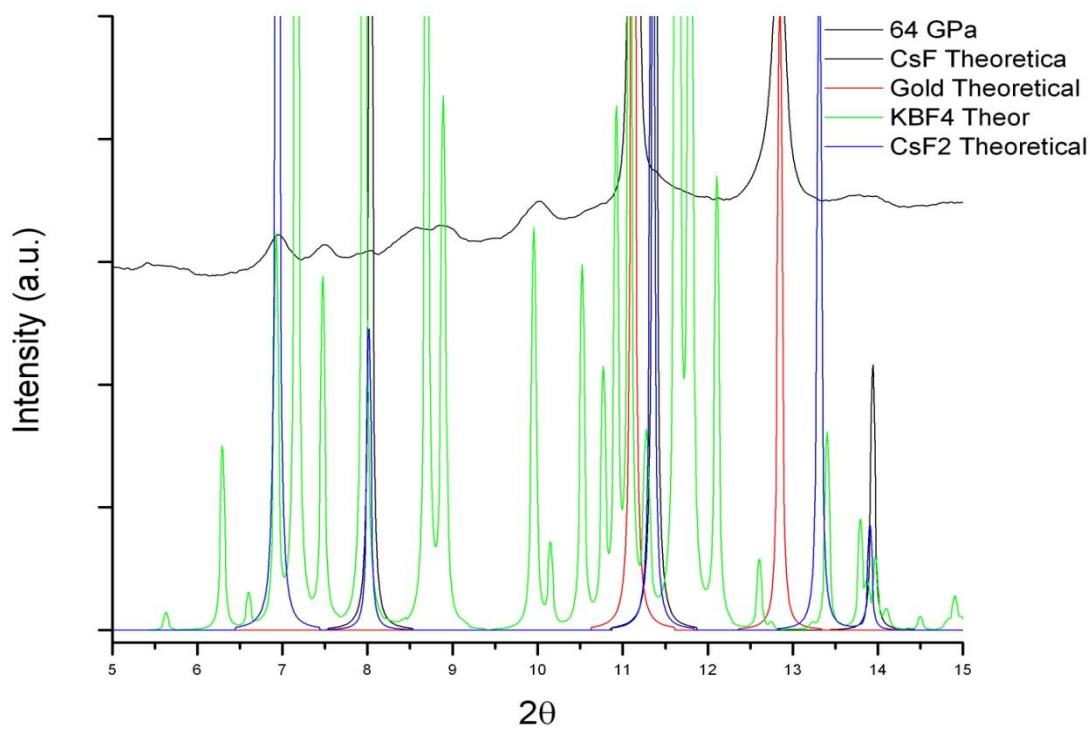


Figure 5.17: X-ray diffraction pattern taken of the mixture of CsF and KBF₄ at 64 GPa along with patterns of potential compounds modeled via Powdercell®

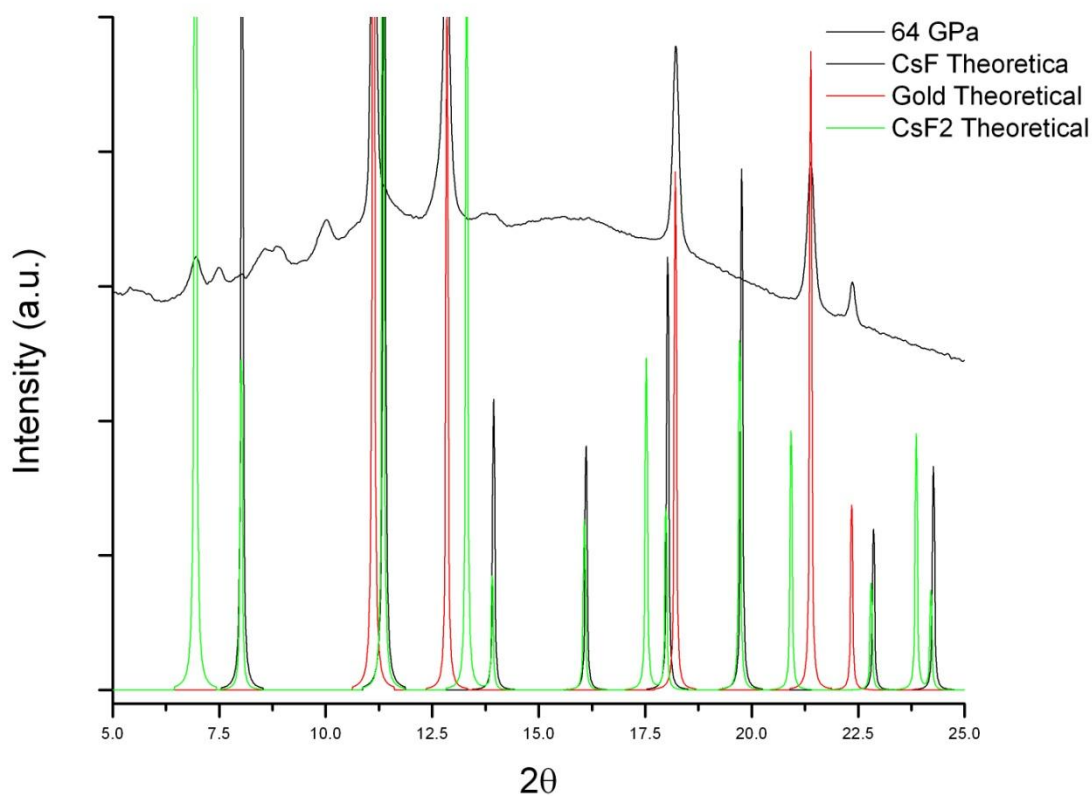


Figure 5.18: X-ray diffraction pattern taken of the mixture of CsF and KBF_4 at 64 GPa along with patterns of potential compounds modeled via Powdercell® without the KBF_4 pattern.

Though CsF_2 in the CaF_2 structure fits to specific peaks with a unit cell parameter ‘a’ of 6.075 \AA , the diffraction data can not conclusively prove that this compound was formed due to the convoluted multiproduct nature of the chemistry experiment.

5.5: Raman study of Potential Novel CsF_n Compound

Raman spectra were recorded of the mixture of CsF and KBF₄ post-decompression from 70 GPa. All modes from the KBF₄ disappeared, and a new mode appears at 125 cm⁻¹, along with a shoulder at 164 cm⁻¹. Comparison spectra were taken of a fresh mixture of CsF and KBF₄ compressed to 3.1 GPa and of pure KBF₄ compressed to 2.3 GPa. An ambient spectrum of pure CsF was also taken as a reference, and all spectra are shown in Figure 5.17. It should be stated that due to the symmetry of the NaCl and CsCl phases, there is no change in polarizability in CsF, therefore it has no active standard Raman modes to the first order. This can also be observed in Figure 5.17.

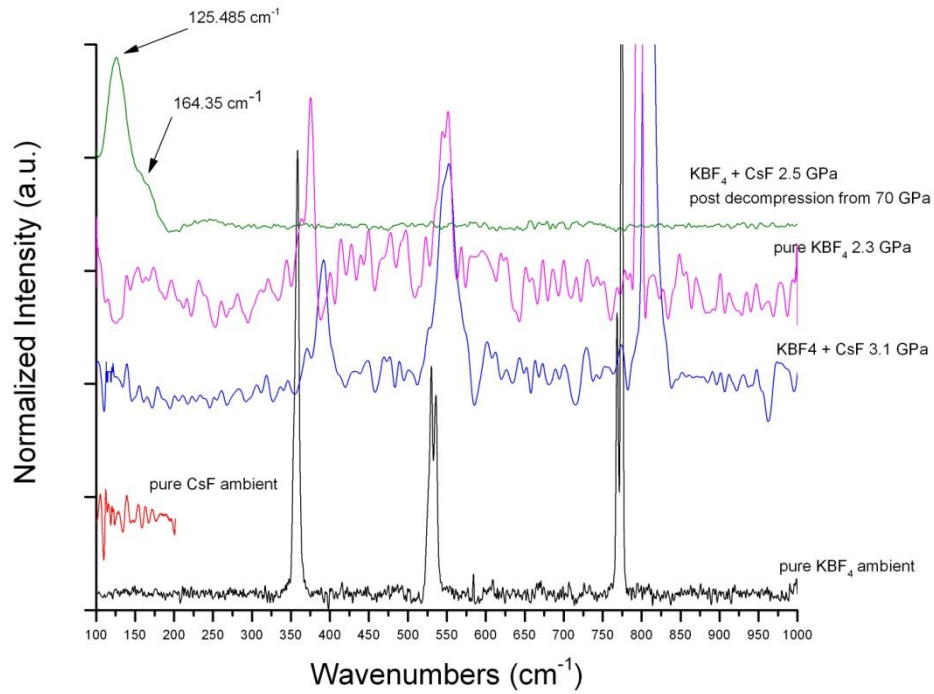


Figure 5.19: Raman spectra of the mixture of KBF₄ and CsF at 2.5 GPa decompressed from 70 GPa showing new modes as compared to control spectra.

Figure 5.18 depicts the potential infrared vibrational modes of the different CsF_n compounds determined via DFT calculations. The active vibrational mode for CsF_2 lies at approximately 185 cm^{-1} , which is slightly higher than the modes shown in Figure 5.17. I believe that this is due to the fact that the DFT calculations were based off of the theoretical prediction that CsF_2 would form as a molecular solid similar to XeF_2 . Despite the theoretical predictions, I believe that the system formed a compound similar to that of CaF_2 , which was discussed further in sections 5.3 and 5.4.

CaF_2 has one primary phonon at approximately 300 cm^{-1} . as cesium is approximately 3 times more massive than calcium, a simple argument can be made that its primary phonon would be on the order of $1/\sqrt{3}$ times lower in energy; this would place it at approximately 165 cm^{-1} , which is near where the shoulder appears in the spectrum in Figure 5.17. It can also be noted that this compound was synthesized at pressures above 65 GPa in conditions that were far from hydrostatic, which can also lead to strain to the lattice and the bonds affecting the phonon energy as well. In CaF_2 , impurities can create other phonon modes as well, which can give an explanation for the mode at 125 cm^{-1} .

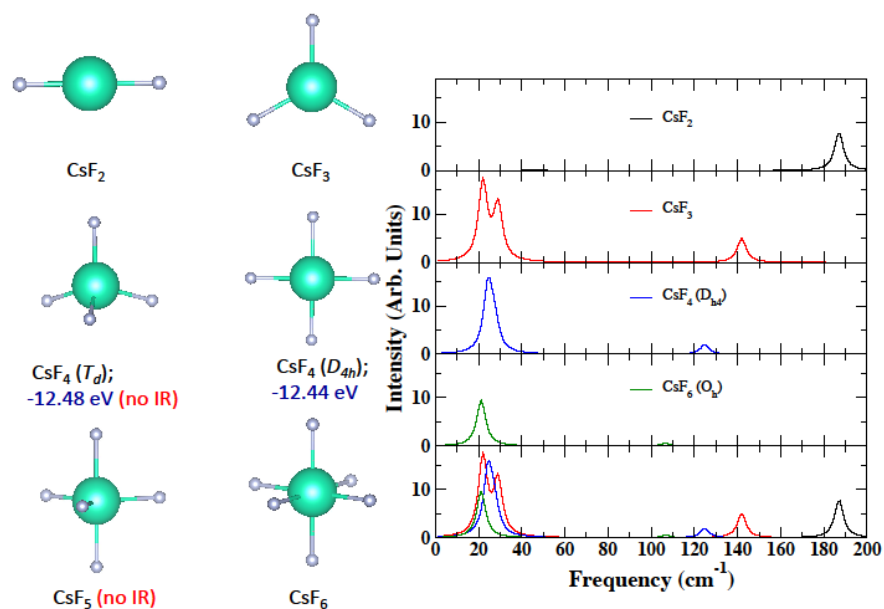


Figure 5.20: The active infrared vibrational modes of the different species of CsF_n compounds determined via DFT calculations.

5.6: Equation of State Measurements of Cesium Fluoride

X-ray diffraction studies of pure cesium fluoride were performed in order to verify the structural stability under high pressures, as well as to determine a non hydrostatic equation of state of its high pressure B2 phase. Figure 5.19 shows pure CsF being pressurized to 18.5 GPa, verifying its phase transition above 5 GPa. The phase transition appears to be sluggish to the mixed phases in the 5.11 GPa pattern. The sample was then decompressed to 3.91 GPa, showing that it did begin to return to its original phase with some hysteresis. The sample pressure was not lowered further for fear of exposing it to air and destroying the sample.

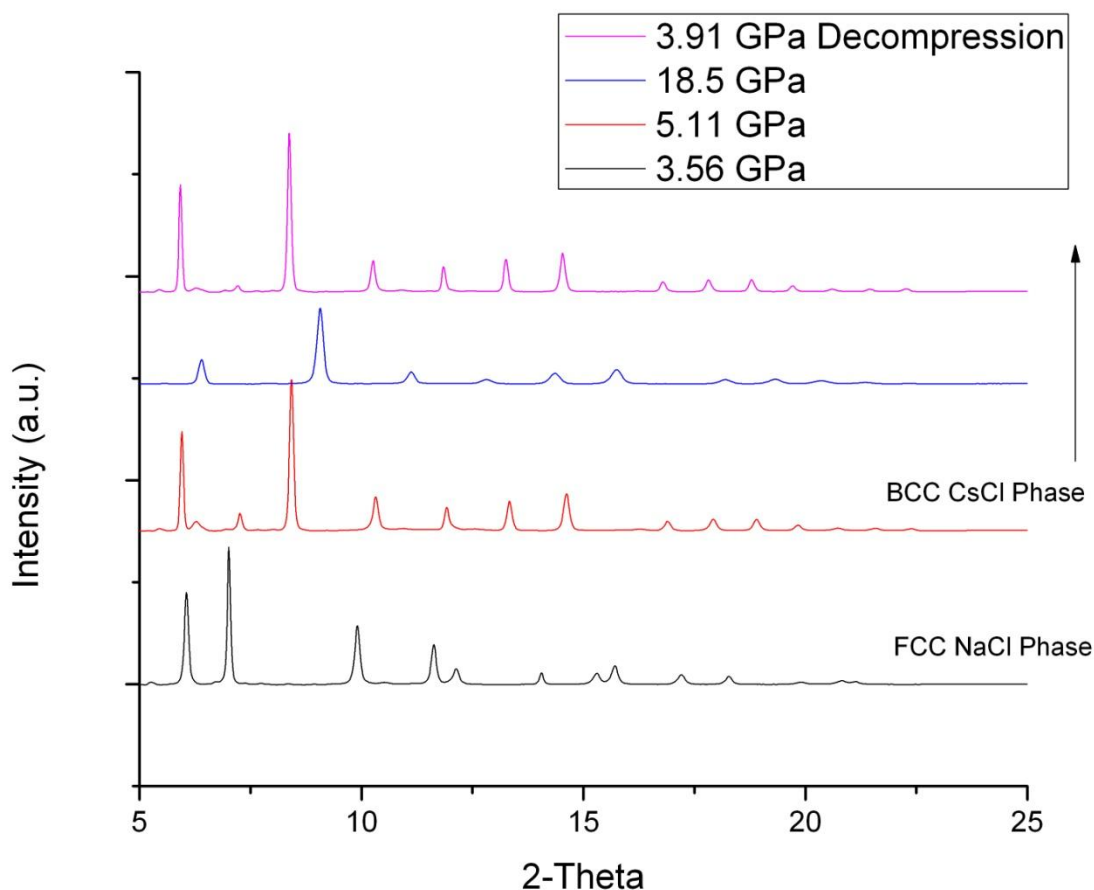


Figure 5.21: X-ray diffraction patterns of pure CsF displaying the phase transition from B1 to B2 above 4 GPa, then decompress back to 3.91 GPa, showing hysteresis.

A new sample of pure CsF was loaded along with a small amount of gold for more accurate pressure measurements and then pressurized to 115 GPa. Figures 5.20 and 5.21 show that, beyond its initial phase transition above 5 GPa, CsF remains in its B2 form up to at least 115 GPa, though it is theoretically stable up to at least 2 Mbar [1].

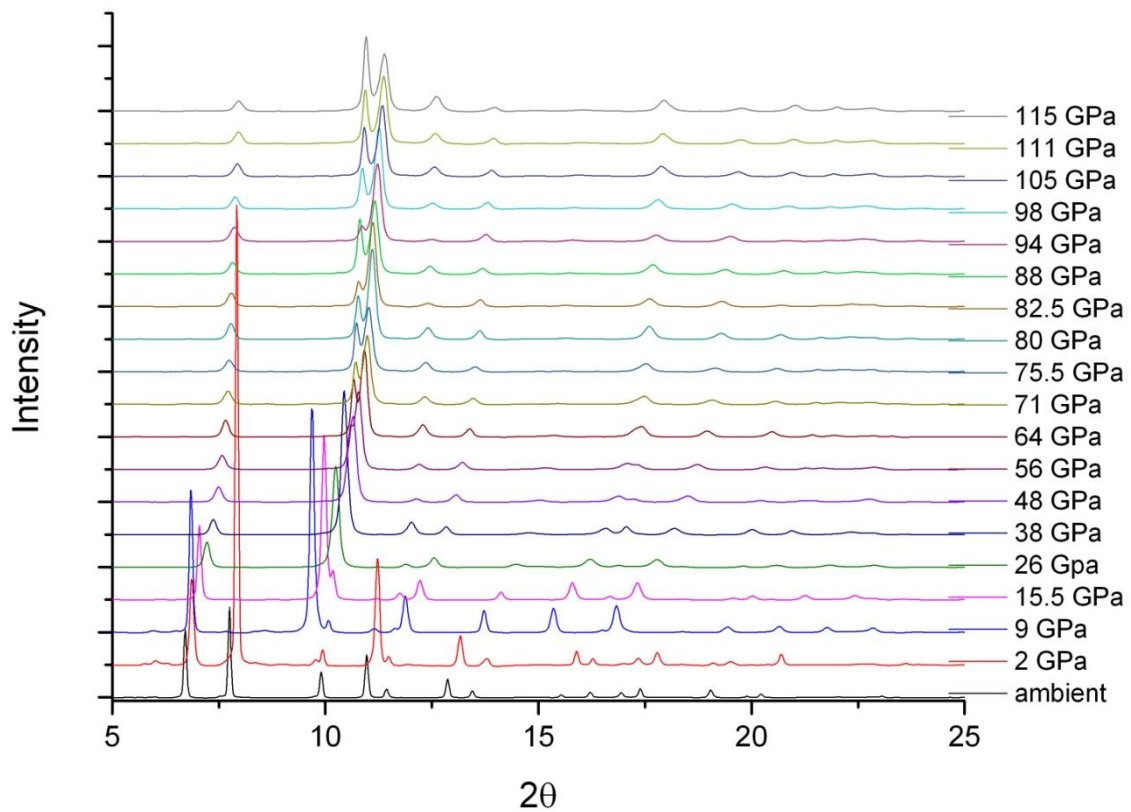


Figure 5.22: X-ray diffraction patterns of pure CsF up to 115 GPa, showing that CsF remains in the B2 phase up to at least 115 GPa.

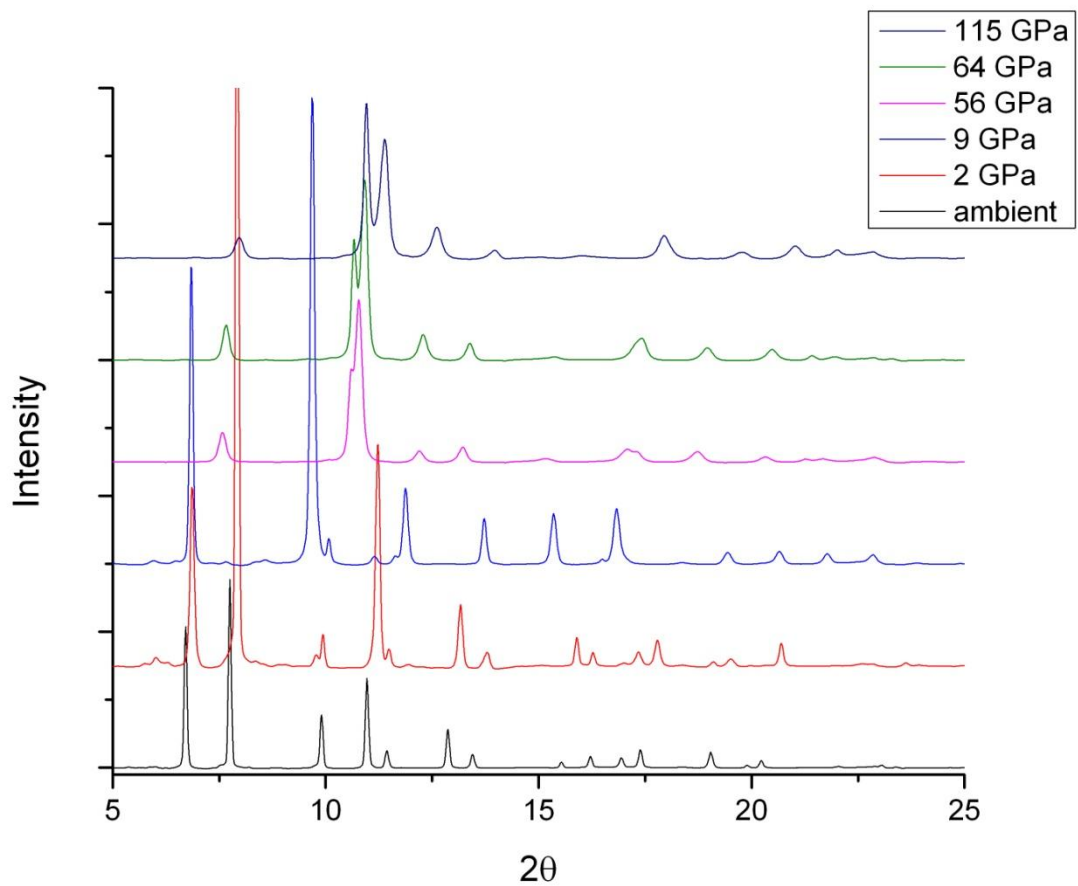


Figure 5.23: Same x-ray diffraction data from figure 5.20 focused around 64 GPa for comparison to XAS experiment.

Table 5.2: Tabulated cell refinement data used for equation of state calculations.

Pressure	Volume	Volume sigma	V/V0	Phase corrected V/V0	sigma Phase corrected V/V0
<i>CsF B1 NaCl phase</i>					
0	219.46	0.0034	1		0.000266147
1.9	203.35	0.0198	0.926592545		0.000262202
<i>CsF B2 CsCl phase</i>					
V_0 (4.7 GPa)	47.91	0.186	0.21831	0.87323	
9.8	39.43	0.0089	0.179668277	0.718673107	6.26375E-05
16.2	36.17	0.0054	0.164813633	0.659254534	5.02298E-05
26.4	33.65	0.0504	0.153330903	0.613323613	0.00023324
36.7	31.47	0.0327	0.14339743	0.57358972	0.000153796
50	29.65	0.0167	0.135104347	0.540417388	8.41377E-05
57.4	28.81	0.0481	0.13127677	0.525107081	0.000221932
67.1	27.61	0.0409	0.125808803	0.503235214	0.000189341
75.1	27.08	0.049	0.123393785	0.493575139	0.00022567
84.4	26.3	0.0391	0.119839606	0.479358425	0.000180987
86.8	26.22	0.0258	0.119475075	0.477900301	0.000121772
90.5	26.09	0.0439	0.118882712	0.475530848	0.000202515
97.9	25.47	0.0368	0.116057596	0.464230384	0.000170496
101.6	25.22	0.0412	0.114918436	0.459673745	0.0001902
108.7	24.69	0.0523	0.112503417	0.45001367	0.00024018
115.5	24.67	0.0422	0.112412285	0.449649139	0.000194596
119.8	24.5	0.0464	0.111637656	0.446550624	0.000213499

From Table 5.2 and Figure 5.21 it is apparent that, once corrected for atoms per unit cell, there is less than a 5% volume collapse across the phase transition from the B1 NaCl fm3m structure to the B2 CsCl pm-3m structure. The B1 phase has 8 atoms per unit cell, whereas the B2 phase has 2 atoms per unit cell. This small volume collapse across the phase transition can also be seen in the XAS data presented in Table 5.1. Though there is a sharp decrease of the unit cell parameter ‘a’ of approximately 50%, the interatomic distances show a smooth systematic decrease of across the phase transition.

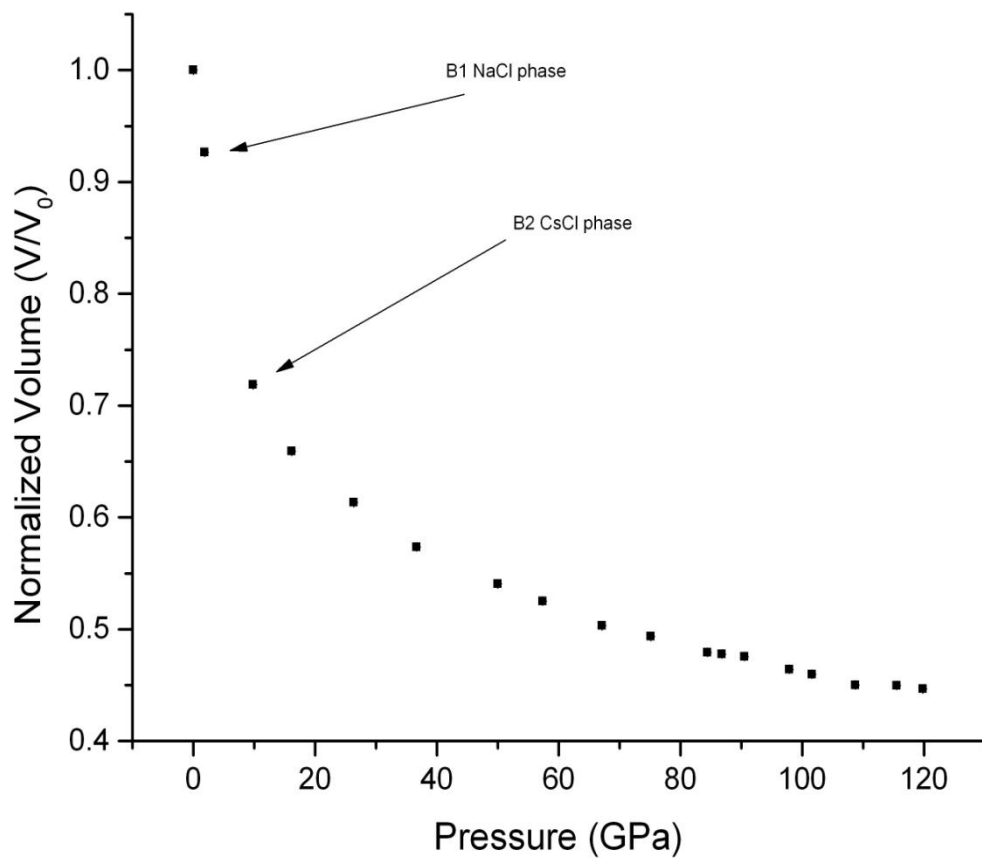


Figure 5.24: Normalized volume as a function of pressure showing slight volume collapse across the B1 to B2 phase transition.

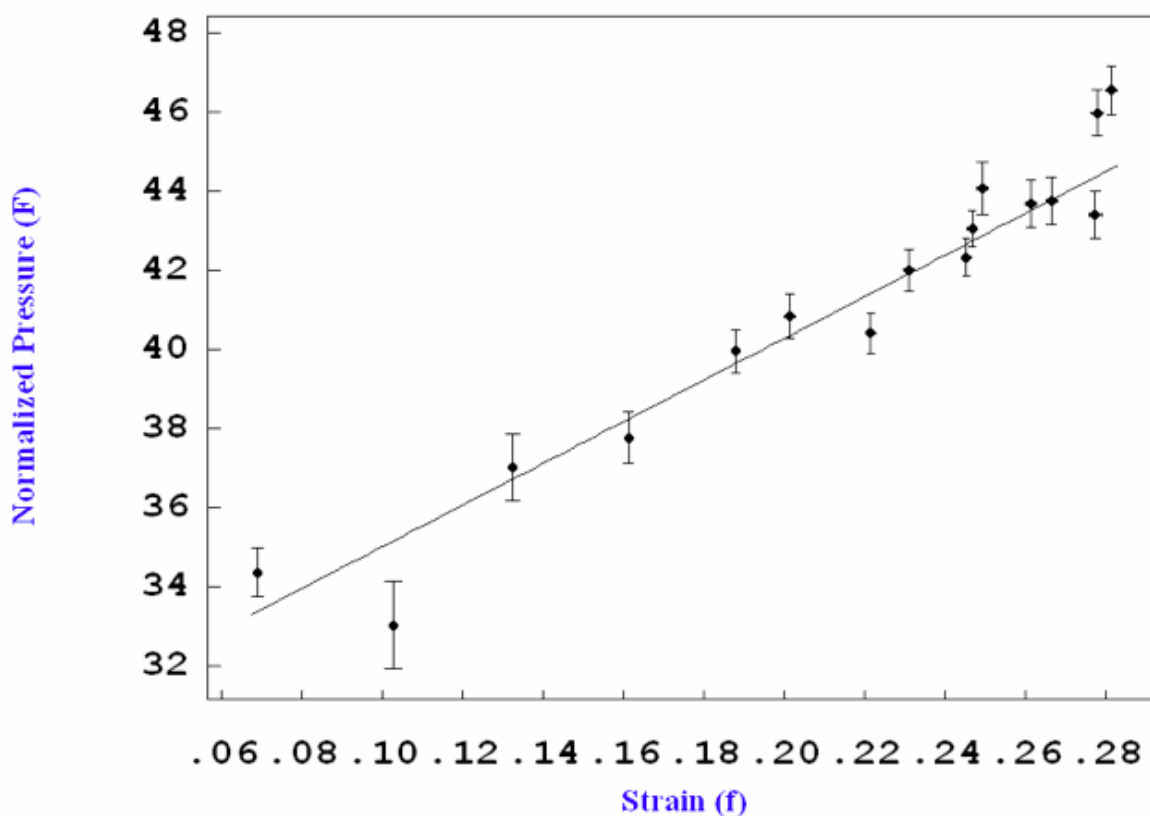


Figure 5.25: Normalized pressure (F) as a function of natural strain (f_E), showing a linear dependence and therefore requiring a 3rd order Birch-Murnaghan equation of state.

As described in section 3.7, in order to determine the order of Birch-Murnaghan equation of state to use to accurately represent your data, the normalized pressure as a function of natural strain, f_E , must be plotted. Using the program EoSfit®, the normalized pressure and natural strain were calculated using the equations discussed in section 3.7 and plotted against each other. Figure 5.22 demonstrates that that this data has a linear relationship between the normalized pressure and the natural strain, suggesting that a 3rd order Birch-Munaghan equation of state must be used to determine the ambient pressure bulk modulus. Figure 5.23 displays the experimental unit cell volume as a function of pressure, along with DFT calculated unit cell volumes and unit cell volumes determined from XAS experiments. DFT calculations give a bulk modulus of 31.84

GPa which agrees extremely well with the experimentally determined value of 29.75 ± 1.28 GPa.

It can also be seen from Figure 5.23 that the values determined from the XAS experiments fall within 10% of the values determined from x-ray diffraction, showing a fairly good agreement between experiments.

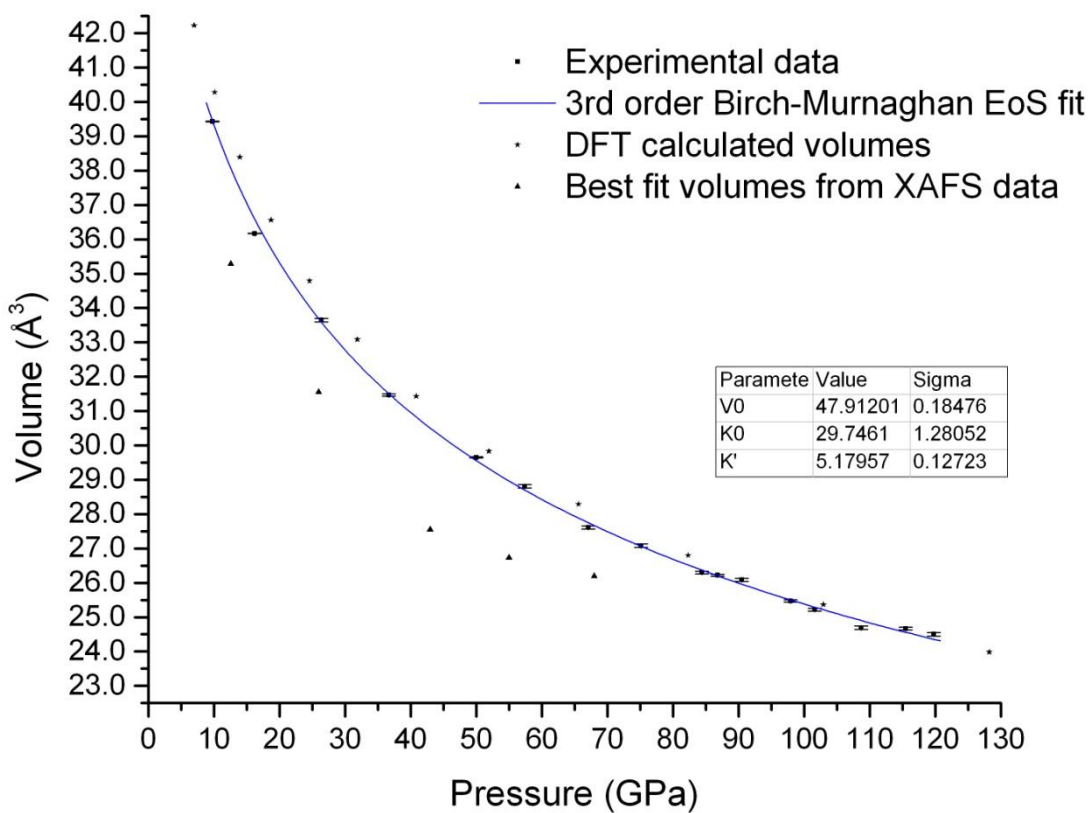


Figure 5.26: Experimental equation of state data compared to both DFT calculated data and volumes determined from XAFS data.

Chapter 6

Conclusions

X-ray absorption spectroscopy was performed on an irradiated mixture of CsF and KBF₄ at pressures up to 70 GPa in an attempt to verify the synthesis of novel CsF_n compounds. Readily evident changes to both the XANES and EXAFS spectra indicate that a possible new compound was synthesized at pressures above 60 GPa. Similarities in the XAS spectra of the new compound to the low pressure B1 phase spectra of pure CsF suggest that this new compound was formed in a cubic type structure, the most likely candidate is CsF₂ in the CaF₂ structure. DFT based modeling was performed on the XAS data in order to attempt to verify and learn about this potential new compound. It did appear to fit as CsF₂ in the CaF₂ structure, though the unit cell parameter 'a' was found to be 7 Å, approximately 40% bigger than the theoretical unit cell parameter of 5.4 Å. Despite this discrepancy, the similarities in the k and R space transforms of the XAS data suggest very similar local coordination's between the new compound and the B1 phase of pure CsF. Another possible compound synthesized in these experiments is KCsF₂, based on the presence of the salt KF via the decomposition of KBF₄. Adding in the cubic KF to the cubic unit cell of CsF via pressure could form a new cubic structure similar to that of KF and CsF, but with a potentially larger unit cell due to the presence of both K and Cs. Though this is one possible compound, further investigation and modeling is needed to verify either way. Though the XANES data did not clearly show a change in oxidation state, it did show that there is a definitive change to the electronic environment, as well as the coordination environment of the cesium atoms. Raman spectra were also taken of the sample showing new modes at 125 and

165 cm^{-1} in the mixture post decompression from 70 GPa, giving further evidence of novel chemistry.

X-ray diffraction of the mixture was recorded, but was extremely convoluted due to the remnants of multiple phases in the sample chamber post reaction. Though CsF_2 could be fit to peaks in the patterns, there still remains too much uncertainty in the patterns to be able to definitively identify all of the potential species in the sample.

XAS was also performed on pure CsF up to 70 GPa to be used as a reference, and a verification that CsF does not undergo any such abrupt changes to its XANES or EXAFS spectra. It was shown that there is a systematic change to the interatomic distances in CsF across its phase transition from its B1 NaCl to B2 CsCl phase, and the change to the unit cell parameter 'a' fits well with data obtained via x-ray diffraction.

X-ray diffraction was performed on pure CsF up to 115 GPa in an attempt to verify the stability of CsF at the pressures reached in the chemistry experiments, as well as to determine a non hydrostatic equation of state of the B2 phase of CsF. A 3rd order Birch-Murnaghan equation of state was used to determine the bulk modulus of the B2 phase of CsF. A K_0 of 29.75 ± 1.28 GPa was calculated, which agrees very well with the theoretical prediction of 31.84 GPa.

References

- 1) Gardiner, D.J. "Practical Raman spectroscopy". Springer-Verlag. ISBN 978-0-387-50254-0. (1989)
- 2) "Raman Spectroscopy", <http://cambridgeforecast.wordpress.com/2006/10/11/raman-spectroscopy/>
- 3) D. W. Hahn, "Raman Scattering Theory" *Department of Mechanical and Aerospace Engineering, University of Florida*, February 2007
- 4) Khanna, R.K. (1981). *J. Chem. Phys.*, **74** (4): 2108.
- 5) M. K. Denk, "Chem 2070 – Structure and Spectroscopy", university of Guelph (2005)
- 6) Smithsonian National Museum of Natural History, "High Pressure Laboratory", <http://mineralsciences.si.edu/facilities/highpressure.htm>
- 7) L. Lei, B. Yan, X. Ji-An, *Chinese Physics B*, **22**, 5, 056201 (2013)
- 8) Argonne National Laboratory, Advanced Photon Source, "A new Gas Loading System for Diamond Anvil Cells at GSECARS"
http://www.aps.anl.gov/News/APS_News/Content/APS_NEWS_20080311B.php (2008)
- 9) Miao M., *Nature Chem.* Vol 5 pp 846-852 (2013)
- 10) Pravica M., Popov D., Sinogeikin S., Sneed D., Guardala G., Smith Q., *Applied Phys. Letters* (2013)
- 11) Pravica M., Sneed D., Smith Q., Bai L., *Chem. Phys. Letters*, **590**, pp 74-76 (2013)
- 12) Pravica M., Sneed D., White M., Wang Y., *Review of Scientific Instruments*, **85**, 086110 (2014)
- 13) Pravica M., Sneed D., White M., Wang Y., *J. Chem. Phys.*, **141** 091101 (2014)

- 14) Pravica M., Liu Y., Bai L., *Chem. Phys. Letters*, **555** pp 113-115 (2013)
- 15) Pravica M., White M., Wang Y., “A novel method for generating molecular mixtures at extreme conditions: The case of fluorine and oxygen” Accepted for publication, *APS SCCM conference proceedings* (2015).
- 16) Merrill Leo, *Journal of Physical and Chemical Reference Data*, **6**, pp. 1205-1252 (1977)
- 17) Pravica *et al*, *Cogent Physics* (2016)
- 18) <http://smb.slac.stanford.edu/~ellis/Thesis/Chapter1.pdf>
- 19) Fabbis G., Lim J., Veiga L.S.I., Haskel D., Schilling J.S., *Phys. Rev. B*, **91**, 085111 (2015)
- 20) https://en.wikipedia.org/wiki/Boron_monofluoride
- 21) Pravica M., Wang Y., Sneed D., Reiser S., White M., “High Pressure Studies of KClO_4 ”, submitted for publication (2016)
- 22) https://en.wikipedia.org/wiki/Caesium_fluoride
- 23) Moszynski M., Gresset C., Vacher J., Odru R., *Nuclear Instruments and Methods*, **179**, 2, pp. 271-276 (1981)
- 24) http://en.wikipedia.org/wiki/Diamond_anvil_cell
- 25) <https://geoweb.princeton.edu/research/MineralPhy/labtour/Ruby.html>
- 26) Gao R., Li H., Zhao J., *American Mineralogist*, **100**, pp 1554-1561 (2015)
- 27) <https://courses.cit.cornell.edu/mse5470/handout4.pdf>
- 28) http://www.theory.nipne.ro/~dragos/Solid/Bravais_table.jpg
- 29) Angel R.J., “Equations of State”,
<http://rimg.geoscienceworld.org/content/gsrmg/41/1/35.full.pdf>

- 30) Bunker G., “X-ray Absorption Spectroscopy”,
<http://gbxafs.iit.edu/training/XAFS%20intro.pdf>
- 31) Newville M., “Fundamentals of XAFS”,
http://xafs.org/Tutorials?action=AttachFile&do=view&target=Newville_xas_fundamentals.pdf
- 32) http://esilrch1.esi.umontreal.ca/~syguschj/cours/BCM6200/Diffractions_Basics.pdf
- 33) <http://www.esrf.eu/about/synchrotron-science/synchrotron>
- 34) http://chemwiki.ucdavis.edu/Core/Physical_Chemistry/Spectroscopy/X-ray_Spectroscopy/XANES%3A_Theory
- 35) http://www.iucr.org/_data/assets/pdf_file/0004/60637/IUCr2011-XAFS-Tutorial_-_Ascone.pdf
- 36) <http://smb.slac.stanford.edu/facilities/hardware/detectors/mar345.html>
- 37) https://en.wikipedia.org/wiki/Calcium_fluoride
- 38) Weir, C.E.; Piermarini, G., *Journal of Research of the National Bureau of Standards, Section A. Physics and Chemistry*, **68**, p105-p111 (1964)

Curriculum Vitae

Daniel Sneed

2381 S Mallard Ave

Pahrump, NV 89048

Phone: (702) 354-7237

Email: sneedd3@unlv.nevada.edu

Education:

Great Basin College	Computer Information Technology	A.A.S. Network Engineering (6/2010)
University Of Nevada, Las Vegas	Physics and Astronomy	B.S. Physics (8/2014)
University of Nevada, Las Vegas	Physics and Astronomy	Masters in Physics (8/2014-present)

Professional Experience:

NSSC Summer Research Fellow	Physical and Life Sciences, Lawrence Livermore National Lab	06/2015-08/2015
Graduate Assistant/Masters Student	Physics and Astronomy Department, University of Nevada Las Vegas Dr. Michael Pravica	08/2014-present
Undergraduate Research Assistant	High Pressure Science and Engineering Center (HiPSEC), University of Nevada Las Vegas Dr. Michael Pravica	03/2012-08/2014
Undergraduate Research Assistant	Physics and Astronomy Department, University of Nevada Las Vegas Dr. John Farley	4/2011-8/2012

Research Experience:

1. Conducted studies into potential impurities in Cadmium Zinc Telluride using Raman spectroscopy and angle dispersed X-ray Diffraction.

2. Conducted High Pressure High Temperature study of Urea using energy dispersed x-ray diffraction at Argonne National Labs Advanced Photon Source, Sector 16 BM-B.
3. Designed, constructed, and operated Raman spectrometer for the High Pressure Science and Engineering Center at the University of Nevada, Las Vegas.
4. Conducted high pressure infrared studies of hexafluorobenzene and carbon tetrachloride at the Canadian Light Source at the University of Saskatchewan in Saskatoon.
5. Conducted X-ray Absorption Fine Structure Spectroscopy (XAFS) studies of cesium fluoride at Argonne National Labs Advanced Photon Source, Sector 16 BM-D
6. Designed and constructed a ruby fluorescence spectrometer for high pressure calibration measurements at the Canadian Light Source.
7. Aided in the design of solid state neutron detectors for use with organic plastic scintillators under Dr. Andrew Glenn and Dr. Natalia Zaitseva at Lawrence Livermore National Lab.
8. Performed Nuclear Assay training at Los Alamos National Lab

Certifications:

1. Radiological Worker I certified, 15 June 2015

Publications:

1. "Measurement of the Energy Dependence of X-ray Induced Decomposition of Potassium Chlorate," M. Pravica, D. Sneed, L. Bai, C. Park, *Journal of Applied Crystallography* (2013)
2. "Studies of carbon tetrachloride at extreme conditions," M. Pravica, D. Sneed, Y. Wang, Q. Smith, and G. Subrahmanyam, *Journal of Chemical Physics*, 140, 194503 (2014)
3. "X-ray induced mobility of molecular oxygen at extreme conditions," Michael Pravica, Dmitry Popov, Stanislav Sinogeikin, Daniel Sneed, Griffin Guardala, and Quinlan Smith, *Applied Physics Letters* (2013)
4. "Effect of Pressure and Temperature on Structural Stability of MoS₂", Nirup Bandaru, Ravhi S. Kumar, Daniel Sneed, Oliver Tschauner, Jason Baker, Daniel Antonio, Sheng-Nian Luo, Thomas Hartmann, Yusheng Zhao, and Rama Venkat, *J. Phys. Chem. C*, 2014, 118 (6), pp 3230–3235 (2014)
5. "High pressure X-ray photochemical studies of carbon tetrachloride: Cl₂ production and segregation," Michael Pravica, Daniel Sneed, Quinlan Smith, and Ligang Bai, *Chemical Physics Letters*, Volume 590, 18 December 2013, Pages 74-76
6. "Note: Loading method of molecular fluorine using x-ray induced chemistry," M. Pravica, D. Sneed, M. White, and Y. Wang, *Review of Scientific Instruments*, 85, 086110 (2014)
7. "Communication: A novel method for generating molecular mixtures at extreme conditions: The case of hydrogen and oxygen," M. Pravica, D. Sneed, M. White, and Y. Wang, *The Journal of Chemical Physics*, 141, 091101 (2014)
8. "Pressure induced structural transitions in CuSbS₂ and CuSbSe₂ thermoelectric compounds," J Baker, R Kumar, D Sneed, A Connolly, Y Zhang, N Velisavljevic, J Paladugu, M Pravica, C Chen, A Cornelius, Y Zhao, *Journal of Alloys and Compounds*, Volume 643, 15 September 2015, Pages 186-194

9. "Forcing Cesium into Higher Oxidation States Using Useful hard x-ray Induced Chemistry under High Pressure," D Sneed, M Pravica, E Kim, N Chen, C Park, M White, *IOP Conference Proceedings*, Submitted for review 30 November 2015

Presentations:

1. "Studies in useful hard x-ray induced chemistry" APS-AIRAPT joint conference, Seattle, WA, July 11 2013
2. "Studies in Useful hard x-ray induced chemistry: Urea and CCl₄ under extreme conditions" Poster presentation at the APS-AIRAPT joint conference, Seattle, WA, July 7, 2013
3. "Studies in Useful hard x-ray induced chemistry: Urea and CCl₄ under extreme conditions" Poster presentation at the 2013 Stewardship Science Academic Programs (SSAP) Annual review symposium, Albuquerque, NM, June 27, 2013
4. "Studies of Molecular Diffusion Under Extreme Conditions", Poster presentation at the 2014 Stewardship Science Academic Programs (SSAP) Annual review symposium, Bethesda, MD, February 19, 2014
5. "Forcing Cesium into Higher Oxidation States Using Useful Hard X-ray Induced Photochemistry at Extreme Conditions" Joint AIRAPT-25 and EHPRG-53 conference, Madrid, Spain, 3 September 2015

Awards

1. First undergraduate to receive outstanding poster award for poster titled "Studies of Molecular Diffusion Under Extreme Conditions" at the 2014 Stewardship Science Academic Programs (SSAP) Annual review symposium, Bethesda, MD, 19 February, 2014
2. Awarded Outstanding poster for poster titled "Forcing Cesium into Higher Oxidation States Using Useful X-Ray Induced Photochemistry at Extreme Pressures" at the 2015 Stewardship Science Academic Programs (SSAP) annual review symposium, Santa Fe, NM, 12 March 2015
3. Awarded NSSC Minority Serving Institutes Summer Research Fellowship, June 2015
4. Awarded travel scholarship to attend the Joint AIRAPT-25 and EHPRG-53 conference, Madrid, Spain, 30 April 2015